LANGMUIR

pubs.acs.org/Langmuir Article

Evolution and Shape of Two-Dimensional Stokesian Drops under the Action of Surface Tension and Electric Field: Linear and Nonlinear Theory and Experiment

Rafael Granda, Jevon Plog, Gen Li, Vitaliy Yurkiv, Farzad Mashayek, and Alexander L. Yarin*



Cite This: Langmuir 2021, 37, 11429-11446



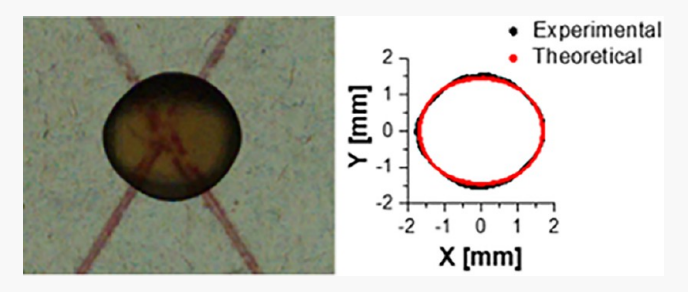
ACCESS I

III Metrics & More



Supporting Information

ABSTRACT: The creeping-flow theory describing evolution and steady-state shape of two-dimensional ionic-conductor drops under the action of surface tension and the subcritical (in terms of the electric Bond number) electric field imposed in the substrate plane is developed. On the other hand, the experimental data are acquired for drops impacted or softly deposited on dielectric surfaces of different wettability and subjected to an in-plane subcritical electric field. Even though the experimental situation involves viscous friction of drops with the substrates and wettability-driven motion of the contact line, the comparison to



the theory reveals that it can accurately describe the steady-state drop shape on a non-wettable substrate. In the latter case, the drop is sufficiently raised above the substrate, which diminishes the three-dimensional effects, making the two-dimensional description (lacking the no-slip condition at the substrate and wettability-driven motion of the contact line) relevant. Accordingly, it is demonstrated how the subcritical electric field deforms the initially circular drops until an elongated steady-state configuration is reached. In particular, the surface tension tends to round off the non-circular drops stretched by the electric Maxwell stresses imposed by the electrodes. A more pronounced substrate wettability leads to more elongated steady-state configurations observed experimentally than those predicted by the two-dimensional theory. The latter cases reveal significant three-dimensional effects in the electrically driven drop stretching. In the supercritical electric fields (corresponding to the supercritical electric Bond numbers), the electrical stretching of drops predicted by the present linearized two-dimensional theory results in splitting into two separate droplets. This scenario is corroborated by the predictions of the fully nonlinear results for similar electrically stretched bubbles in the creeping-flow regime available in the literature as well as by the present experimental results on a substrate with slip.

1. INTRODUCTION

Electrowetting (EW) is of interest in a wide range of applications and involves significant fundamental aspects. 1-4 Control of drop deposition on a solid surface is important for numerous industrial processes. In particular, EW allows for an active switching between wettable and non-wettable surface states without changing the liquid and surface properties. Moreover, drop deposition and spraying in many cases aim at enhanced spreading and reduction or complete suppression of drop splashing and bouncing.5 This can be achieved by employing EW controlled by electrodes attached to the substrate. 6,7 Similar situations emerge in spray-painting and spray-cooling applications. An applied electric field also facilitates drop motion over dielectric substrates in threedimensional (3D) printing⁸ or jet deposition on uneven substrates in direct writing applications⁹ as well as can enhance adhesion of deposited solidified liquid to the substrate. 10

The physical reason for EW is the rapid motion of ions (always present in liquids^{5,11,12}) toward the underneath substrate as a result of the electrical migration caused by the Coulomb force attracting them to the substrate parts of

opposite polarity. Then, the surface tension (surface energy) at the substrate—liquid interface is diminished from its original value corresponding to the case without the electric field by the value of the electric energy of ions accumulated at the interface. This is because the ions repel each other. Accordingly, in the presence of the electric field, the Young equation transforms into the Young—Lippmann equation, which describes how the contact angle diminishes as a result of the action of the electric field applied; i.e., the substrate becomes more wettable.^{2–5,8} The decrease in the equilibrium contact angle modifies the dynamics of drop spreading¹³ and can facilitate drop coalescence on dielectric solid substrates with embedded electrodes.^{9,14–16}

Received: April 14, 2021 Published: September 24, 2021





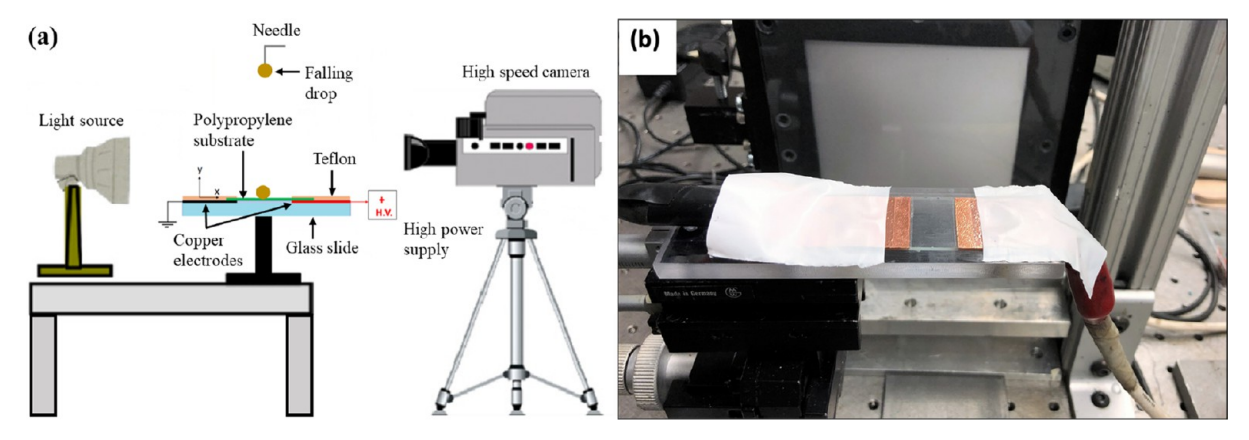


Figure 1. (a) Schematic of the experimental setup for studying drop impact and its electrically driven evolution and (b) image of the experimental setup.

The key element in the evolution of the drop shape under the action of the applied electric field is the competition of the stretching electric Maxwell stresses acting at the drop surface with the restoring surface tension, which is accompanied by viscous dissipation inside the drop (assuming that the process is slow and the inertial effects are negligibly small). It is worth theoretical exploration of these mechanisms first considering a two-dimensional (2D) "free" drop and avoiding complications related to the presence of a substrate (the three-phase contact line and the overall three-dimensionality of the problem). The 2D flows in 2D drops and around 2D bubbles can be described by solutions of the biharmonic equation for the stream function, 17,18 which yields powerful theoretical tools available for such problems. The theoretical approach used in the present work dates back to the method developed in ref 19 (cf. ref 12) and based on solution of the biharmonic equation for the stream function with linearized boundary conditions. Even though linearized, such solutions reveal an amazing accuracy far outside of their formal range of validity, as shown by comparison to the experimental data in ref 19 in the case when only surface tension and no electric field is involved. Here, a comparison to the experimental and numerical data of the present work is also used to verify the accuracy of the analytical results obtained.

In principle, another approach based on the complexization of the planar Stokes equations of creeping flows promises analytical solutions of fully nonlinear problems; albeit, some form of linearization could still be very handy when dealing with the electric-field-related effects. Historically, this approach originated in the theory of elasticity, contact problems, and fracture mechanics, which effectively employed the general solution of the biharmonic equation for the Airy stress function in the form of the Goursat formula with the complex elastic potentials. More recently, this approach was used in the 2D Stokesian fluid mechanics, because the 2D flows in 2D drops and around 2D bubbles can be reduced to the biharmonic equation for the stream function as, for example, in refs 29–41.

In the present work, drops on a dielectric substrate under the action of the electric field are experimentally studied in section 2, where the experimental setup is described, and in section 3, which presents the experimental findings. Then, the 2D "free" drop model is pursued, and the electric Maxwell stresses at the drop surface are calculated in section 4. The subsequent section 5 describes the transient viscous creeping flow in the interior of the 2D "free" drop under the action of the Maxwell stresses and surface tension. Section 6 is devoted to the subcritical (in terms of the electric Bond number) case, where a steady-state drop shape is found analytically. Section 7 presents several examples of the results of the linearized theory of sections 4–6, including steady-state non-circular configurations and transient evolution up to the drop rupture by the electric forces. It also includes comparison of the linearized theory with nonlinear numerical results. Section 8 describes the comparison of the experimental data to the theoretical predictions, i.e., is devoted to the results and discussion. Conclusions are drawn in section 9.

2. EXPERIMENTAL SETUP

Two types of experiments were conducted. In the first type, drops impacted onto the dielectric substrate were released from a certain height. The substrate was subjected to the electric field by two inplane electrodes, and the drop evolution upon its impact in the middle of the substrate was recorded. In the second type of experiments, a drop was softly deposited on the dielectric substrate, then the electric field was applied by two in-plane electrodes, and the resulting drop evolution was recorded.

The setup for the experiments of the first type is illustrated in Figure 1. A polypropylene film was overlaid over a glass slide and used as the dielectric substrate for drop impact and evolution. Two in-plane electrodes made of a copper tape were overlaid onto the substrate at a distance of 1.5 cm from each other, with the polypropylene film in between being the working space. In addition, the polypropylene film was carefully cut as a 2 cm (length) \times 2 cm (width) piece placed above the two in-plane copper electrodes. Over the electrodes, the polypropylene surface was insulated by Teflon. One of the electrodes was connected to a positive high-voltage direct current (DC) supply (EL40P1, Glassman High Voltage, Inc., custom built with a 0–20 kV range). The other copper electrode was grounded.

The glass slide with the polypropylene substrate on top of it equipped with the electrodes was mounted on the adjustable platform, which could be controlled in three directions, in particular, changing the height between the tip of the needle, which released a drop, and the solid surface (cf. Figure 1). Additionally, a fine-tune control along one of the horizontal axes allowed one to aim the center of the drop impact at the interelectrode center. For this particular case, a needle exit height of h=12.5 cm was kept constant throughout the experiments with and without the applied voltage. The average impact velocity was 1.50 m/s, as measured from the video recording, which is slightly lower (probably as a result of the effect of the air drag) than the estimate of $\sqrt{2gh}=1.57$ m/s, where g is the gravity acceleration.

Water mixed with water-soluble gold oak aniline dye (0.1 wt % concentration) was used as the working fluid in all of the experiments.

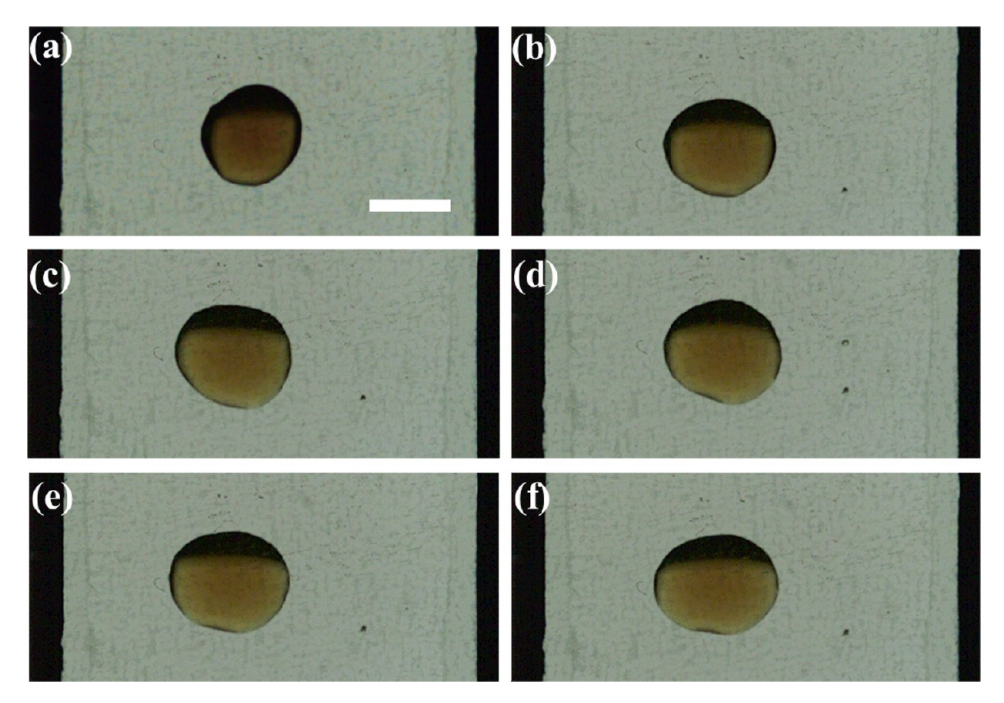


Figure 2. Steady-state drop shapes after drop impact onto the polypropylene substrate without an electric field and under the action of the electric field: (a) 0 kV, (b) 4.5 kV, (c) 5 kV, (d) 7 kV, (e) 9 kV, and (f) 10 kV. The left-hand-side electrode is the anode, and the right-hand-side electrode is grounded (the cathode). The scale bar is 3 mm.

A laboratory syringe pump (NE-1000 Series) supplied the liquid to a 90° bent 27-gauge needle at a flow rate of 6 mL/h. The out-of-focus 90° bent 27-gauge needle helped place the camera right above the needle to visualize the top view in the drop impact. The average drop diameters were about 2.5 mm when the 27-gauge needle was used. The drops detached and fell onto the polypropylene substrate as a result of gravity, and hence, the impact velocity was controlled by the height of the needle exit with respect to the plane solid surface. Only a normal drop impact was studied here.

In additional experiments, glycerol was used as a working fluid.

To visualize the side and top views of drop impact and evolution simultaneously, two high-speed cameras (Phantom V210 and Phantom Miro 4) were set up. For the side viewing, back lighting [light-emitting diode (LED) lamp] illuminated the drop, and for the top viewing, front lighting was used. In recording the side views, the camera was aligned at the same vertical level as that of the polypropylene substrate. The images were analyzed in Adobe Photoshop, MATLAB, and ImageJ. The impact velocity was determined by the drop motion observed in the side view. All measurements and experiments were performed at room temperature.

The experimental setup used for the experiments of the second type was similar to that of Figure 1. Here, either polypropylene or parafilm films were used as the dielectric substrates. In either case, polypropylene or parafilm was carefully cut into 2 cm (length) × 2 cm (width) pieces placed above the two in-plane electrodes (made of a copper tape) similarly to the experiment of the first type. The area between the electrodes was used for the experiments with the drop evolution on either polypropylene or parafilm surfaces. The distance between the electrodes was reduced to 1 cm. Outside of the electrodes, both substrate surfaces were insulated by Teflon. The polypropylene or parafilm films with the overlaid electrodes and Teflon insulation were stuck on a microscope glass slide. One of the electrodes was connected to a positive high-voltage DC supply (EL40P1, Glassman High Voltage, Inc., custom built with a 0-20 kV range). The other copper electrode was grounded. Note that Teflon was used to insulate the electrodes from the liquid drops and prevent a short circuit. Hence, the drops are only in contact with the dielectric layer after drop impact or after being softly deposited. The Teflon film was used as a safety measure when performing the experiments, especially at higher applied voltages.

As in the experiments of the first type, the glass slide with either one of the substrates equipped with the electrodes was mounted on the adjustable platform, which could be controlled in three directions, and another adjustable platform with a fine-tuning three-axes control was used to aim the center of the dielectric surface at the interelectrode center and softly place the sessile drop from the bent needle. The same working fluid was used as in the experiments of the first type.

3. EXPERIMENTAL RESULTS

3.1. Drop Impact Case. Single drops of water mixed with aniline dye dripped onto the polypropylene substrate from a fixed height of 12.5 cm. The top view recorded by a high-speed camera captured the collision and evolution of drops at a rate of 1000 fps. Figure 2a depicts the recorded steady-state shapes achieved by the drop after it impacted onto the polypropylene surface when no electric field was applied, whereas the steady-state shapes achieved by the drop with DC voltage applied are shown in panels b—f of Figure 2. The average diameter of each drop before the impact was \sim 2.5 mm, and the impact velocity was 1.50 m/s in all cases.

The steady-state drop contour traces corresponding to the observations in Figure 2 are depicted in Figure 3. The superposition of the drop shape contours without the electric field (at 0 kV) and with application of different DC voltages (4.5, 5, 7, 9, and 10 kV, with the corresponding electric field strengths of 3.0×10^5 , 3.33×10^5 , 4.67×10^5 , 6.0×10^5 , and 6.67×10^5 V/m, respectively) reveals the effect of the electric force on the drop shape, with the maximum drop stretching corresponding to the case of 10 kV. The applied electric field stretches the drop along the substrate (in the direction of the field lines), and its steady-state footprint area slightly increases as the electric field strength increases, as shown in Table 1. As a result of the liquid incompressibility, this means that the drop as a layer becomes thinner under the action of the electric field in comparison to the case without an electric field. It should be

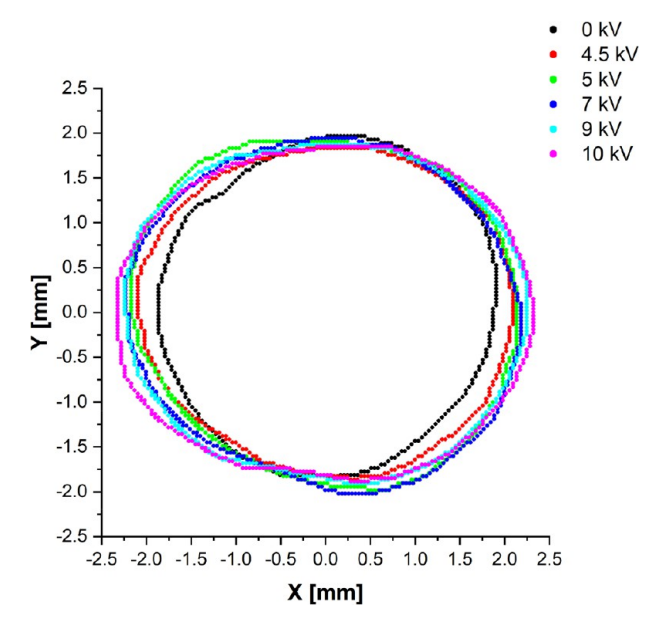


Figure 3. Steady-state drop contours of a single drop of water with aniline dye after drop impact onto the polypropylene substrate without and with the action of the electric field. The left-hand-side electrode is the anode, and the right-hand-side electrode is grounded (the cathode). The Cartesian coordinates on the substrate are denoted as x (in the field direction) and y.

Table 1. Steady-State Footprint Areas of a Single Water—Aniline Dye Drop Recorded after Drop Impact onto the Polypropylene Substrate without and with the Applied Voltage

case	area (mm²)
0 kV	11.02
4.5 kV	12.01
5 kV	13.27
7 kV	13.33
9 kV	13.44
10 kV	13.75

emphasized that the area increase recorded in Table 1 is a purely 3D effect, which cannot be described by a purely 2D theory attempted below in this work. It is noteworthy that drops did not acquire their original footprint after switching off the high-power supply. This occurred at all of the voltages applied to the dielectric substrate. Such a non-returning effect presumably reveals the hidden effect of the substrate roughness on the receding motion of the contact line, which could be pinned by roughness.

The centers of the drops analyzed in Figure 3 are very close in all cases presented, which simplifies the analysis of the steady-state footprint contours obtained from the top view. The stretching by the electric force is counteracted by the surface tension, and in transition to a steady state of a drop (in the cases of subcritical electric fields, as those in Figures 2 and 3), the power supplied by the electric field is partially "invested" in an increase in the surface energy and partially spent for viscous dissipation.

3.2. Softly Deposited Drop Case. Here, single drops of water mixed with aniline dye were softly placed on the polypropylene and parafilm substrates. The top views recorded by a high-speed camera at a rate of 500 fps captured the evolution of the drops when the electric field was applied.

Figure 4 depicts the recorded steady-state shapes of a sessile drop on the polypropylene surface when no voltage was applied (the left-hand-side column) and with DC voltage applied (the right-hand-side column). The same drop is depicted in each row (with no voltage applied, as shown on the left) and then after voltage has been applied and a steady state has been reached (as shown on the right). Thus, each panel in Figure 4 allows for a direct comparison between the drop shape before and after voltage has been applied on the substrate.

Additional experiments on the polypropylene substrate were conducted at lower voltages (4.5, 5, and 6 kV). However, only the 6 kV voltage revealed some effect (drop stretching in the x direction, i.e., the field direction) on the sessile drop, as shown in Figure 5. The top view recorded by a high-speed camera captured, at a rate of 500 fps, the evolution of the drop after the 6 kV voltage was applied. In this case, special efforts were taken to initially place the drop center right at the substrate center marked by the center of the cross intersection (cf. Figure 5 on the left). The steady-state drop is still shifted to some extent from the center (cf. Figure 5 on the right), which attests to a certain asymmetry of the electric field.

Furthermore, Figure 6 depicts the recorded steady-state shapes of a sessile drop on a parafilm surface when no voltage was applied (the left-hand-side column) and with DC voltage applied (the right-hand-side column), similar to those shown in Figures 4 and 5. It should be emphasized that each panel in Figure 6 allows for a direct comparison between the drop shape before (on the left-hand side) and after (on the right-hand side) voltage has been applied.

The steady-state drop contour traces observed on the polypropylene substrate corresponding to the images in Figures 4 and 5 are depicted in Figure 7. The superposition of the contour measured without voltage application with those measured at voltages of 6, 7, 9, 10, and 10.5 kV (with electric field strengths of 6×10^5 , 7×10^5 , 9×10^5 , 10×10^5 , and 10.5×10^5 V/m, respectively) reveals the effect of the electric forces on the drop shape. The maximum stretching along the field lines corresponds to the case of 10.5 kV shown in Figure 7e.

When the electric field strength is relatively small (panels a and b of Figure 7), drop stretching is relatively small. On the other hand, at the higher field strengths, panels c—e of Figure 7 reveal a significant drop stretching, especially pronounced in the 10.5 kV case. The repeatability of the results on the electrically driven drop stretching after it was softly deposited on the polypropylene substrate was tested in the additional experiments at the three highest voltages, and the results are superimposed with those of Figure 7 in Figure 8. The comparison in Figure 8 reveals a reasonable repeatability, which slightly deteriorates at the highest voltage studied.

The average footprint surface areas measured in the top views of Figure 7 along with the additional trials of Figure 8 are presented in Table 2. The area increase observed in Table 2 is a purely 3D effect.

The steady-state drop contours measured on the parafilm substrate corresponding to the experimental observations in Figure 6 are depicted in Figure 9. They reveal drop stretching by the electric field at the applied voltages of 8, 9, 10, and 10.5 kV (with electric field strengths of 8×10^5 , 9×10^5 , 10×10^5 , and 10.5×10^5 V/m, respectively). Unlike the experimental results shown in Figures 7 and 8 (the polypropylene surface), the results obtained on the parafilm are quite different. Here,

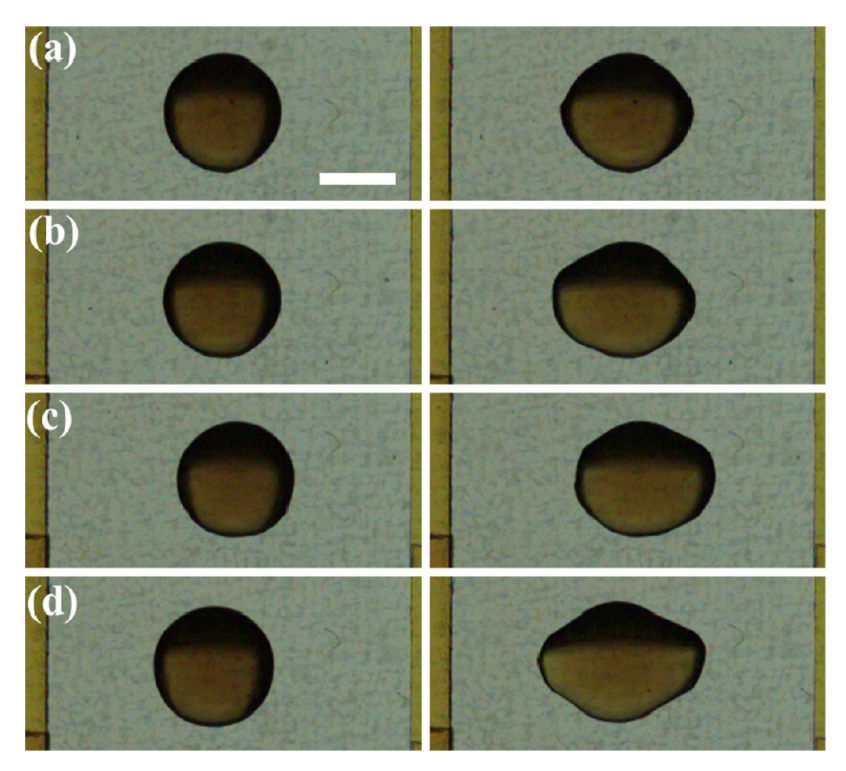


Figure 4. Steady-state drop shapes on the polypropylene substrate under the action of the electric field. Left-hand-side column, no voltage applied; right-hand-side column, applied voltages of (a) 7 kV, (b) 9 kV, (c) 10 kV, and (d) 10.5 kV (with corresponding electric field strengths of 7×10^5 , 9×10^5 , 9×10^5 , 9×10^5 , and 9×10^5 , 9×10^5 , 9×10^5 , and 9×10^5 , and 9×10^5 , 9×10^5 , 9×10^5 , and 9×10^5

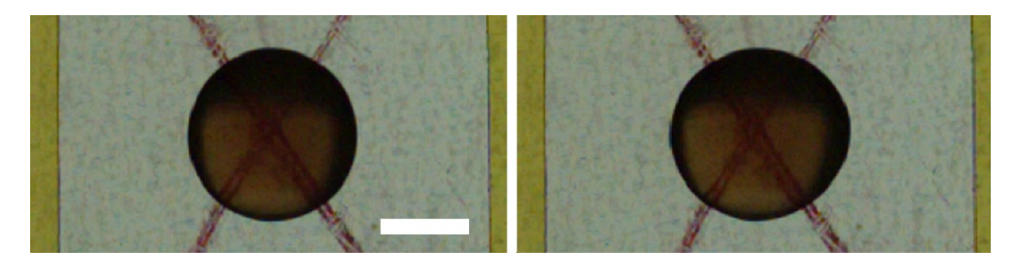


Figure 5. Steady-state drop shapes on the polypropylene substrate under the action of the electric field. Left-hand-side column, no voltage applied; right-hand-side column, 6 kV voltage applied (with the electric field strength of 6×10^5 V/m). The left-hand-side electrode is the anode, and the right-hand-side electrode is grounded (the cathode). The drop center is roughly at the cross intersection. The scale bar is 2 mm.

the stretching along the field lines is almost unnoticeable at 8 kV (Figure 9a). At 9, 10, and 10.5 kV corresponding to panels b—d of Figure 9, the drop stretching is still significantly smaller than those for the corresponding voltages applied to a drop on the polypropylene substrate. It should be emphasized that these experiments were repeatable in multiple trials for each applied voltage, and the data shown here are representative trials used to demonstrate the results. The comparison of Figures 7 and 9 clearly shows that the observed drop stretching depends upon the substrate material, presumably its wettability by the liquid of the drop. The difference in the substrate wettability is determined by the difference in the molecular interactions of the liquid and the substrate, the substrate roughness, and the severity of the EW phenomenon on it.

The steady-state footprint surface areas measured from Figure 9 are listed in Table 3. The areas measured without and with applied voltage are practically indistinguishable in these cases. Therefore, the 3D effect is practically immaterial here, and a comparison with the 2D theory developed below is more justifiable.

The choice of the substrates is determined by potential importance of substrate wettability. To characterize the effect of different wettability of polypropylene and parafilm surfaces on the behavior of water-aniline dye drops, the equilibrium contact angles were measured without voltage applied, and the results are compared in Figure S1 of the Supporting Information. Characterization of surface wettability by the equilibrium contact angle is quite standard. 13 Accordingly, the polypropylene surface is more hydrophilic (the contact angle is less than 90°, i.e., 84.8° in Figure S1a of the Supporting Information), whereas the parafilm surface is more hydrophobic (the contact angle is more than 90°, i.e., 100.4° in Figure S1b of the Supporting Information). Additional measurements revealed that the contact angles gradually decreased as the applied voltage increased for both surfaces (in accordance with the Young-Lippmann equation). In particular, the contact angle decreased from 84.8° at 0 kV to 68.2° at 10.5 kV for the polypropylene substrate and from 100.4° at 0 kV to 82.7° at 10.5 kV for the parafilm substrate. The subsequent trials revealed a secondary dependence of

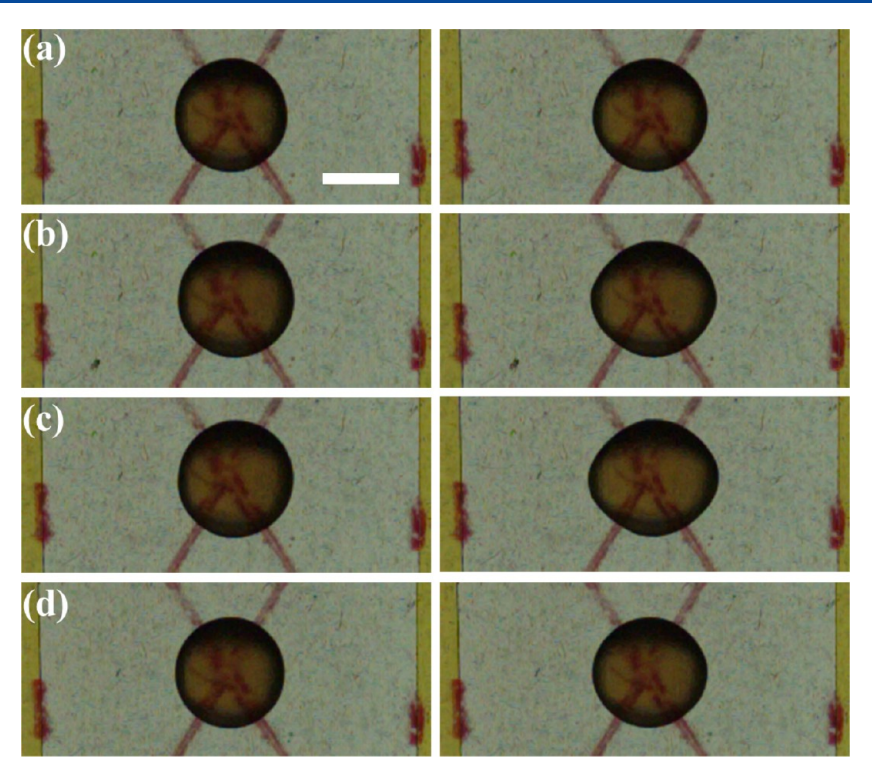


Figure 6. Steady-state drop shapes achieved under the action of the electric field on the parafilm substrate. Left-hand-side column, no voltage applied; right-hand-side column, shapes achieved with applied voltages of (a) 8 kV, (b) 9 kV, (c) 10 kV, and (d) 10.5 kV (with corresponding electric field strengths of 8×10^5 , 9×10^5 , 10×10^5 , and 10.5×10^5 V/m, respectively). The left-hand-side electrode is the anode, and the right-hand-side electrode is grounded (the cathode). The drop center is roughly at the cross intersection. The scale bar is 2 mm.

these results upon, presumably, the surface roughness. Note that another widely used material relevant to EW is Teflon. It is reported that Teflon reveals a static contact angle with water of $96 \pm 4^{\circ}$, which decreases to $78 \pm 3^{\circ}$ when a 6 kV voltage is applied. This range of contact angle is within the range covered by the cases of polypropylene (more hydrophilic) and parafilm (more hydrophobic).

It should be emphasized that the outcome is dependent upon the microstructure of the substrate, which could be inadvertently altered by the trapped liquid because consecutive trials were conducted on the same substrate. Hence, the substrate roughness and wettability could also be modified as a result of the presence of trapped liquid, with the receding motion of the contact line arrested, while drops pinned at the substrate.

4. ELECTRIC MAXWELL STRESS AT THE DROP SURFACE

Consider a 2D liquid drop subjected to the electric field with the strength vector directed along the α axis at infinity. The drop is considered to be a perfect conductor, i.e., equipotential, with the electric potential being 0 (without the loss of generality because of the arbitrary addable constant). In the case of ionic conductors, the approximation of a perfect conductor is appropriate when the charge relaxation time is much shorter than the characteristic hydrodynamic time associated with the rate of the evolution of the drop shape under the action of the electric field and capillarity. Note also that the drops considered here are originally electroneutral and do not possess a charge, as those in the seminal works of Rayleigh and the following works. Also, the present drops do not experience shearing electric tractions at their surfaces

and the associated internal circulations or electrorotation, as the experiments reveal, which makes the situation here radically different from those considered (mostly for nonplanar spherical or spheroidal cases) in the literature. $^{44-49}$

The drop shape is described in the polar coordinates as

$$R(\theta, t) = R_0[1 + \varepsilon Z(\theta, t)] \tag{4.1}$$

where R_0 is the unperturbed (initial) drop radius and εZ is its dimensionless perturbation, which depends upon the polar angle θ and time t. Note that it is implied that ε is a small parameter, formally much less than 1, whereas Z is of the order of 1.

Equation 4.1 shows that here small deformations of a drop relative to the initial circular shape are sought, albeit relaxation of the requirement of such smallness would be aimed in comparison to the experimental data. Because the stretching electric force on the order of 1 acts even on an unperturbed circular drop, the rate of stretching could be high, even without shape perturbations (at Z = 0) or when such perturbations are still small. As a consequence, even though the shape perturbations can grow relatively fast, there is a period of time when they are still small. That is exactly the period of time of interest here. During this time period, linearization would be possible, and thus, a linearized theory could be developed, as below. In the inertialess approximation (the creeping flow) of interest here, the following four physical parameters govern the problem: the unperturbed (initial) drop radius R_0 , the viscosity and surface tension of liquid μ and σ , respectively, and the electric field strength E_{∞} . Keeping in mind the CGS system of units, these four parameters incorporate three independent units, and thus, according to the Buckingham π theorem, ^{50,51}

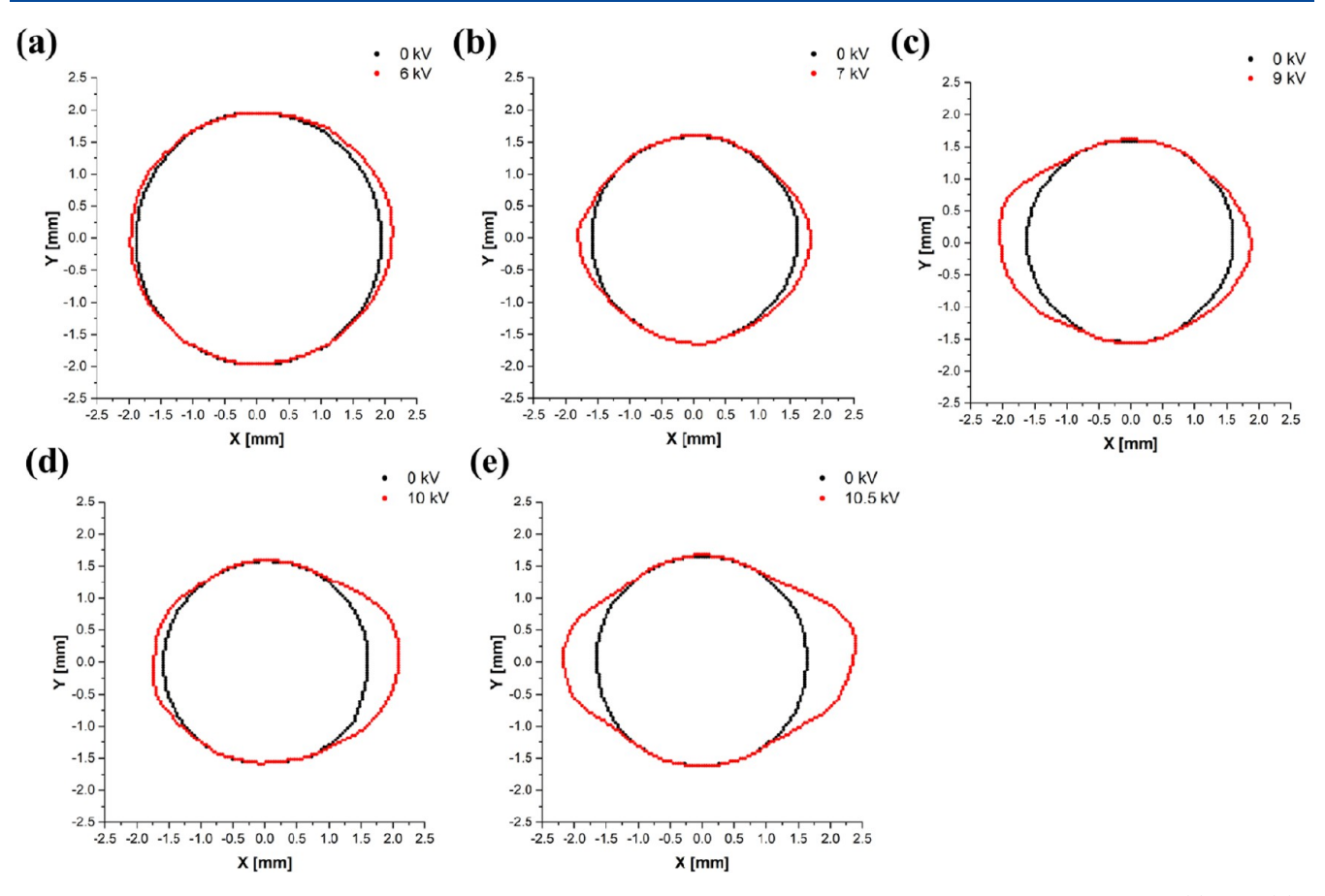


Figure 7. Steady-state water—aniline dye drop contours measured on the polypropylene substrate without and with electric fields of (a) 6 kV, (b) 7 kV, (c) 9 kV, (d) 10 kV, and (e) 10.5 kV. The left-hand-side electrode is the anode, and the right-hand-side electrode is grounded (the cathode). The Cartesian coordinates on the substrate are denoted as *x* (in the field direction) and *y*.

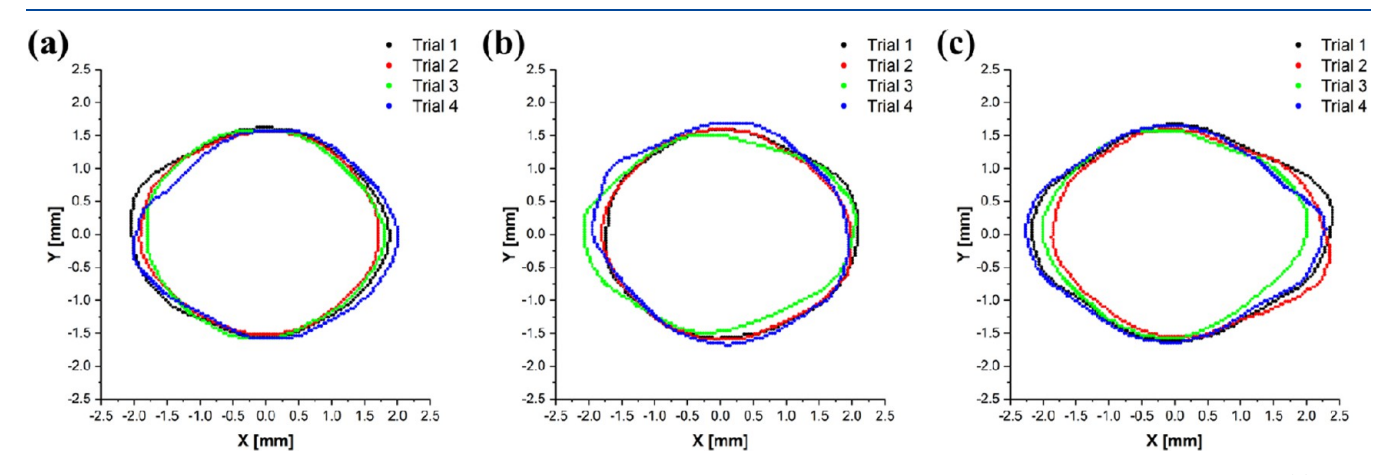


Figure 8. Steady-state water—aniline dye drop contours measured on the polypropylene substrate without and with the electric field of (a) 9 kV, (b) 10 kV, and (c) 10.5 kV. The left-hand-side electrode is the anode, and the right-hand-side electrode is grounded (the cathode). The Cartesian coordinates on the substrate are denoted as x (in the field direction) and y. Trial 1 corresponds to Figure 7, and trials 2–4 result from additional experiments.

there is a single dimensionless group, the electric Bond number, given by the following expression:

$$Bo_{E} = \frac{E_{\infty}^{2} R_{0}}{\sigma} \tag{4.2}$$

The duration of time when perturbations are small enough is, accordingly, dictated by the dimensional considerations as $t < (\mu R_0/\sigma) f(\mathrm{Bo_E})$, where $f(\mathrm{Bo_E})$ is the dimensionless function of

the electric Bond number. One can expect that the time period shortens when the electric field strength increases, and thus, $f(\mathrm{Bo_E}) \sim 1/\mathrm{Bo_E}$, and accordingly, the time period when shape perturbations are small is $t < \mu R_0/\sigma \mathrm{Bo_E}$. A more accurate estimate is derived *a posteriori*, as discussed in relation to eq 5.19, namely

Table 2. Steady-State Average Footprint Areas of a Single Water—Aniline Dye Drop Recorded on the Polypropylene Substrate without and with the Applied Voltage

case	no voltage (mm²)	with applied voltage (mm²)
6 kV	11.52 ± 0.42	12.20 ± 0.41
7 kV	8.07 ± 0.11	8.57 ± 0.41
9 kV	7.77 ± 0.32	8.90 ± 0.44
10 kV	8.06 ± 0.08	9.33 ± 0.39
10.5 kV	8.01 ± 0.48	10.08 ± 0.85

$$t < 12\pi \frac{\mu R_0}{\sigma Bo_E} \tag{4.3}$$

Note also that in a subcritical field (in terms of the electric Bond number) drop evolution can come to a steady state, in which stretching by the electric field (by the Maxwell stresses at the surface) is compensated pointwise by the capillary pressure associated with the surface tension. If, in such a case, the drop distortion compared to its initial circular shape is small, then the time limit of eq 4.3 becomes immaterial and the linearized small deformation description sought here is valid indefinitely.

To find the drop shape, one needs to find the timedependent coefficients $c_n(t)$ and $b_n(t)$ in the expansion of the surface perturbation in the Fourier series

$$Z(\theta, t) = \frac{b_0(t)}{2} + \sum_{n=1}^{\infty} \left[c_n(t) \sin n\theta + b_n(t) \cos n\theta \right]$$
(4.4)

where the coefficients are of the order of 1 during the time interval of eq 4.3.

The electric field surrounding the drop is described by the electric potential φ , which is sought as the solution of the Laplace equation in polar coordinates

$$\frac{1}{r}\frac{\partial}{\partial r}\left(r\frac{\partial\varphi}{\partial r}\right) + \frac{1}{r^2}\frac{\partial^2\varphi}{\partial\theta^2} = 0 \tag{4.5}$$

where r is the radial coordinate.

The solution is subjected by the following boundary conditions:

$$\varphi|_{r=R_0(1+\varepsilon Z)} = 0, \quad \left. \frac{\partial \varphi}{\partial r} \right|_{r=\infty} = -E_\infty \cos \theta$$
 (4.6)

The second condition in eq 4.6 stems from the fact that the unperturbed electric field at infinity is parallel to the x axis, i.e.,

Table 3. Steady-State Footprint Areas of a Single Water—Aniline Dye Drop Recorded on the Parafilm Substrate without and with the Applied Voltage

case	no voltage (mm²)	with applied voltage (mm²)
8 kV	7.03	7.08
9 kV	7.45	7.82
10 kV	7.42	8.04
10.5 kV	6.72	6.90

$$\varphi|_{r=\infty} = -E_{\infty}x = -E_{\infty}r\cos\theta \tag{4.7}$$

and it is implied that $E_{\infty} > 0$; i.e., the anode is located at $x = -\infty$, and the cathode is located at $x = \infty$.

The unperturbed solution of $\varphi = \varphi_0$ of eq 4.5 corresponding to the following boundary conditions:

$$\left. \varphi_0 \right|_{r=R_0} = 0, \quad \left. \frac{\partial \varphi_0}{\partial r} \right|_{r=\infty} = -E_\infty \cos \theta$$
(4.8)

reads

$$\varphi_0 = -E_{\infty} r \left(1 - \frac{R_0^2}{r^2} \right) \cos \theta \tag{4.9}$$

This is the order of one electric field (and the corresponding electric field strength) experienced by an initially circular drop. Figure 10 corresponds to the structure of the field lines found using eq 4.9 and the Cauchy-Riemann conditions, which determine the field lines γ (which is related by the Cauchy– Riemann conditions to the electric potential). The electric field vector $\mathbf{E} = -\nabla \varphi$ is directed outward of the drop on the righthand side (x > 0) and inward on the left-hand side (x < 0)because the cathode is at $x = +\infty$ and the anode is at $x = -\infty$. It should be emphasized that then cations are located at the drop surface at x < 0 (on the anode side) and anions are located at the drop surface at x > 0 (on the cathode side). Accordingly, the Coulomb force acting on the drop, which is the product of the surface charge with E, is directed everywhere outward at the drop surface. Therefore, the drop is not only stretched along the x axis (toward the anode and cathode on the left- and right-hand sides, respectively) but is also pulled upward and downward along the y axis.

Because of the stretching, the circular drop will begin to deform, thus perturbing the electric field of Figure 10. The perturbed electric potential can be presented in the following form:

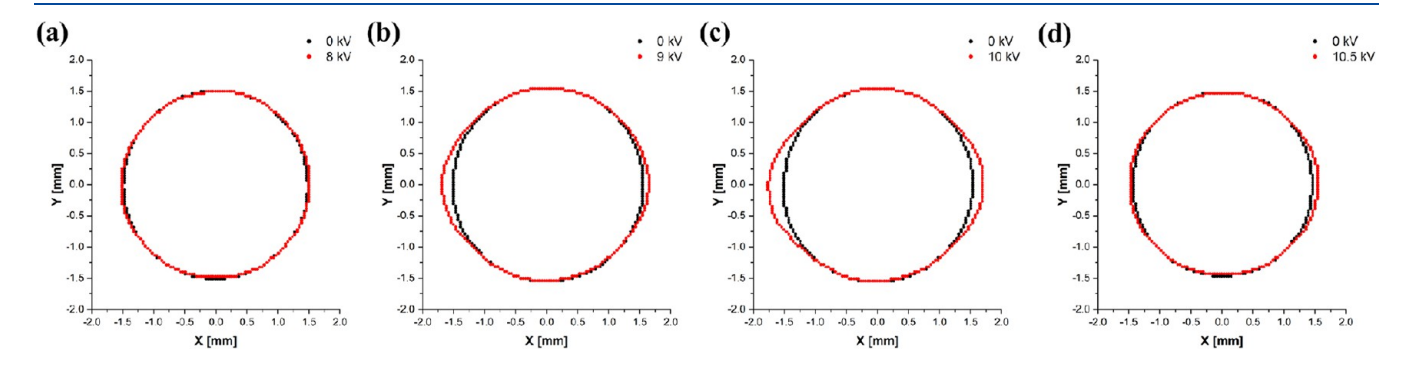


Figure 9. Steady-state water—aniline dye drop contours measured on the parafilm substrate without and with electric fields of (a) 8 kV, (b) 9 kV, (c) 10 kV, and (d) 10.5 kV. The left-hand-side electrode is the anode, and the right-hand-side electrode is grounded (the cathode). The Cartesian coordinates on the substrate are denoted as x (in the field direction) and y.

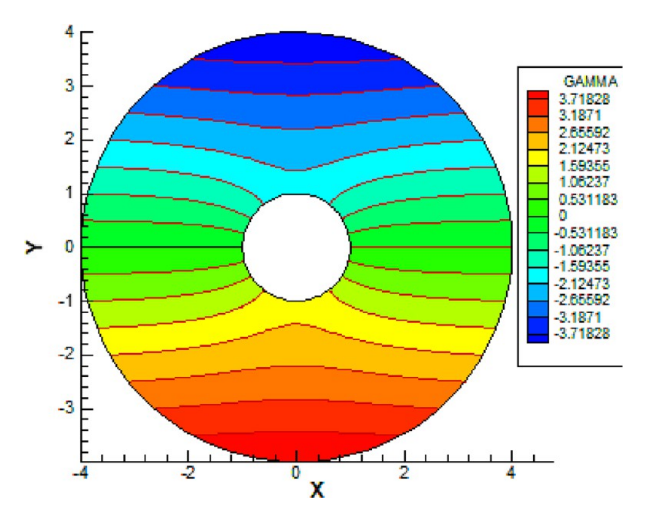


Figure 10. Electric field lines surrounding the original drop occupying the white circle of radius 1 at t=0. The coordinates x and y and the drop radius are rendered dimensionless by R_0 . The corresponding structure of the electric field lines is found via function γ related by the Cauchy–Riemann conditions to the electric potential φ_0 . The line on which γ is a constant is the field line. Note that γ is rendered dimensionless by $E_{\infty}R_0$.

$$\varphi = \varphi_0 + \varepsilon \tilde{\varphi} \tag{4.10}$$

where the perturbation is assumed to be small, while $\tilde{\varphi}$ is of the order of 1. The perturbation of the electric field stems from the perturbation of the drop shape.

The perturbation of the potential is found, according to eqs 4.1, 4.6, 4.8, and 4.9 from the following linearized problem:

$$\frac{1}{r}\frac{\partial}{\partial r}\left(r\frac{\partial\tilde{\varphi}}{\partial r}\right) + \frac{1}{r^2}\frac{\partial^2\tilde{\varphi}}{\partial\theta^2} = 0 \tag{4.11}$$

$$\tilde{\varphi}|_{r=R_0} = -\frac{\partial \varphi_0}{\partial r} \bigg|_{r=R_0} R_0 Z = 2E_{\infty} R_0 \cos \theta Z \tag{4.12}$$

$$\left. \frac{\partial \tilde{\varphi}}{\partial r} \right|_{r=\infty} = 0 \tag{4.13}$$

It should be emphasized that here and hereinafter linearization is used; i.e., only the terms of the order of 1 and $O(\varepsilon)$ are left, whereas the higher orders of ε (ε^2 , etc.) are truncated. In particular, this is done in eq 4.12, which stems from the $O(\varepsilon)$ term in the expansion of the function $\varphi[R_0(1 + \varepsilon Z)]$ in the Taylor series.

The solution of the problem in eqs 4.11-4.13 with Z given by eq 4.4 is found using the method of variable separation in the following form:

$$\tilde{\varphi} = E_{\infty} R_0 \{ b_1 + \frac{R_0}{r} [c_2 \sin \theta + (b_0 + b_2) \cos \theta] + \sum_{n=2}^{\infty} \left(\frac{R_0}{r} \right)^n [(c_{n+1} + c_{n-1}) \sin n\theta + (b_{n+1} + b_{n-1}) \cos n\theta] \}$$
(4.14)

In the linear approximation, the unit tangent vector τ and the outward unit normal vector ν at the drop surface are found as

$$\tau = \mathbf{e}_{\theta} + \mathbf{e}_{r} \varepsilon \frac{\partial Z}{\partial \theta}, \quad \nu = \mathbf{e}_{r} - \mathbf{e}_{\theta} \varepsilon \frac{\partial Z}{\partial \theta}$$
 (4.15)

where \mathbf{e}_r and \mathbf{e}_θ are the unit vectors of the radial and azimuthal directions of the polar coordinate system.

Then, in the linear approximation, the normal component of the electric field strength at the drop surface is found as

$$\begin{split} E_{\nu}|_{r=R_{0}(1+\varepsilon Z)} &= \mathbf{E} \cdot \boldsymbol{\nu}|_{r=R_{0}(1+\varepsilon Z)} \\ &= - \left(\frac{\partial \varphi_{0}}{\partial r} \bigg|_{r=R_{0}} + \frac{\partial^{2} \varphi_{0}}{\partial r^{2}} \bigg|_{r=R_{0}} R_{0} \varepsilon Z \right. \\ &\left. + \left. \varepsilon \frac{\partial \tilde{\varphi}}{\partial r} \right|_{r=R_{0}} \right) \end{split} \tag{4.16}$$

Note that eq 4.16 accounts for the fact that $\partial \varphi_0/\partial \theta|_{r=R_0}=0$. Note also that the tangential component of the electric field strength vector

$$E_{\tau}|_{r=R_0(1+\epsilon Z)} = 0 \tag{4.17}$$

because the drop is a conductor and, thus, equipotential.

The electric Maxwell stress tensor σ^E is related to the electric field strength vector **E** as follows:⁵²

$$\boldsymbol{\sigma}^{\mathrm{E}} = \frac{1}{4\pi} \left(\mathbf{E}\mathbf{E} - \frac{1}{2} |\mathbf{E}|^2 \mathbf{I} \right) \tag{4.18}$$

This expression is written in CGS units, and the unit tensor is denoted as I.

Equations 4.17 and 4.18 yield zero shear stress at the drop surface

$$\sigma_{\nu\tau}^{E}|_{r=R_{0}(1+\varepsilon Z)} = 0 \tag{4.19}$$

whereas the normal stress pulling the drop surface outward is given in the linear approximation according to eqs 4.16 and 4.18 by the following expression:

$$\begin{split} \sigma_{\nu\nu}^{\mathrm{E}}|_{r=R_{0}(1+\varepsilon Z)} &= \frac{1}{8\pi} E_{\nu}^{2}|_{r=R_{0}(1+\varepsilon Z)} \\ &= \frac{1}{8\pi} \left[\left(\frac{\partial \varphi_{0}}{\partial r} \Big|_{r=R_{0}} \right)^{2} + 2 \frac{\partial \varphi_{0}}{\partial r} \Big|_{r=R_{0}} \frac{\partial^{2} \varphi_{0}}{\partial r^{2}} \Big|_{r=R_{0}} \right. \\ &\left. R_{0} \varepsilon Z + 2 \frac{\partial \varphi_{0}}{\partial r} \Big|_{r=R_{0}} \varepsilon \frac{\partial \tilde{\varphi}}{\partial r} \Big|_{r=R_{0}} \right] \end{split}$$
(4.20)

Substituting eqs 4.4, 4.9, and 4.14 into eq 4.20, one obtains the expression for the normal stress at the drop surface as

$$\sigma_{\nu\nu}^{E}|_{r=R_{0}(1+\varepsilon Z)} = \frac{E_{\infty}^{2}}{4\pi} (1 + \cos 2\theta) - \frac{E_{\infty}^{2}}{4\pi} \varepsilon \{ (c_{1} + c_{3})\sin \theta + (3b_{1} + b_{3})\cos \theta + (c_{2} + c_{4})\sin 2\theta + (b_{2} + b_{4}) \\ \cos 2\theta + \sum_{n=3}^{\infty} [(c_{n+2} + 2c_{n} + c_{n-2})\sin n\theta + (b_{n+2} + 2b_{n} + b_{n-2})\cos n\theta] \} \\ + \frac{E_{\infty}^{2}}{4\pi} \varepsilon \left\{ \sum_{n=1}^{\infty} (n+1)[(c_{n+2} + c_{n})\sin n\theta + (b_{n+2} + b_{n})\cos n\theta] + \sum_{n=3}^{\infty} (n-1) \right\}$$

$$[(c_{n} + c_{n-2})\sin n\theta + (b_{n} + b_{n-2})\cos n\theta] \}$$

$$(4.21)$$

It should be emphasized that the first term in eq 4.19 describes the electric stress acting at the unperturbed circular drop (which is of the order of 1), whereas the other terms arise as a result of the perturbations (and are of the order of ε).

Note also that the surface tension at the drop surface causes the capillary pressure $p_{\rm cap}$. In the approximation of small perturbations (the linear approximation) employed here, it reduces to the following expression:

$$p_{\text{cap}} = \frac{\sigma}{R_0} (1 - \varepsilon Z) - \frac{\sigma}{R_0} \varepsilon \frac{\partial^2 Z}{\partial \theta^2}$$
(4.22)

where σ is the surface tension coefficient.

Using eq 4.4, eq 4.22 is transformed to the following form:

$$p_{\text{cap}} = \frac{\sigma}{R_0} + \frac{\sigma}{R_0} \varepsilon \left[-\frac{b_0}{2} + 3c_2 \sin 2\theta + 3b_2 \cos 2\theta + \sum_{n=3}^{\infty} c_n (n^2 - 1) \sin n\theta + b_n (n^2 - 1) \cos n\theta \right]$$
(4.23)

The first term in eq 4.23 describes the capillary pressure acting on the unperturbed circular drop, whereas the other terms arise as a result of the perturbations. The capillary pressure yields the capillary stress

$$\sigma_{\nu\nu}^{\text{cap}}|_{r=R_0(1+\epsilon Z)} = -p_{\text{cap}} \tag{4.24}$$

which will counteract to the electric stress in eq 4.21.

5. VISCOUS CREEPING FLOW IN THE DROP INTERIOR

The general solution of the biharmonic equation for the stream function ψ in polar coordinates given by ref 19 also yields the general expressions for the velocity components and stresses. In the present case, all of the expressions should be finite at r=0, which determines that two of the coefficients of the general expressions found by ref 19 should vanish and the expressions for the viscous stresses important here read

$$\sigma_{rr}^{\text{visc}} = \mu \sum_{n=2}^{\infty} \left[r^n (-2n - 4 + 2n^2) + Dr^{n-2} (2n^2 - 2n) \right]$$

$$(\tilde{A}_n \cos n\theta + \tilde{B}_n \sin n\theta)$$

$$- 4\mu r (\tilde{A}_1 \cos \theta + \tilde{B}_1 \sin \theta) - K$$

$$\sigma_{r\theta}^{\text{visc}} = \mu \sum_{n=2}^{\infty} \left[r^n (-2n^2 - 2n) + Dr^{n-2} (-2n^2 + 2n) \right]$$

$$(\tilde{A}_n \sin n\theta - \tilde{B}_n \cos n\theta)$$

$$- 4\mu r (\tilde{A}_1 \sin \theta - \tilde{B}_1 \cos \theta)$$

$$(5.2)$$

In eqs 5.1 and 5.2, μ is the viscosity and D, K, \tilde{A}_n , and \tilde{B}_n are the functions of time t to be found.

In the linear approximation employed here, according to ref

$$\sigma_{\nu\nu}^{\text{visc}}|_{r=R_0(1+\varepsilon Z)} = \sigma_{rr}^{\text{visc}}|_{r=R_0}, \quad \sigma_{\nu\tau}^{\text{visc}}|_{r=R_0(1+\varepsilon Z)} = \sigma_{r\theta}^{\text{visc}}|_{r=R_0}$$
(5.3)

On the other hand, at the drop surface, the following dynamics boundary conditions for the stresses hold:

$$\begin{aligned}
\sigma_{\nu\nu}^{\text{visc}}|_{r=R_0(1+\epsilon Z)} &= \sigma_{\nu\nu}^{\text{E}}|_{r=R_0(1+\epsilon Z)} + \sigma_{\nu\nu}^{\text{cap}}|_{r=R_0(1+\epsilon Z)}, \\
\sigma_{\nu\tau}^{\text{visc}}|_{r=R_0(1+\epsilon Z)} &= \sigma_{\nu\tau}^{\text{E}}|_{r=R_0(1+\epsilon Z)}
\end{aligned} (5.4)$$

Using eqs 4.19 and 5.2 and the second boundary condition in eq 5.4, one finds

$$D = R_0^2 \frac{(n+1)}{(-n+1)} \tag{5.5}$$

and

$$\tilde{A}_1 = \tilde{B}_1 = 0 \tag{5.6}$$

Equations 4.21, 4.23, 4.24, and 5.1 and the first boundary condition in eq 5.4 yield

$$K = \frac{E_{\infty}^2}{4\pi} - \frac{\sigma}{R_0} + \frac{\sigma}{R_0} \varepsilon \frac{b_0}{2}$$
 (5.7)

$$\frac{E_{\infty}^{2}}{4\pi}\varepsilon(c_{1}+c_{3}) = -4\mu R_{0}\tilde{B}_{1} = 0$$
(5.8)

$$-\frac{E_{\infty}^{2}}{4\pi}\varepsilon(b_{1}-b_{3}) = -4\mu R_{0}\tilde{A}_{1} = 0$$
(5.9)

Note that, in eqs 5.8 and 5.9, eq 5.6 has already been used. Substituting eq 5.5 and 5.6 into eq 5.1, one finds

$$\sigma_{rr}^{\text{visc}}|_{r=R_0} = -4\mu \sum_{n=2}^{\infty} R_0^{\ n} (n+1) (\tilde{A}_n \cos n\theta + \tilde{B}_n \sin n\theta)$$
(5.10)

Then, eqs 4.21, 4.23, 4.24, and 5.10 and the first boundary condition in eq 5.4 yield

$$\tilde{A}_{2} = -\frac{E_{\infty}^{2}}{48\pi\mu R_{0}^{2}} [1 + 2\varepsilon(b_{2} + b_{4})] + \frac{\sigma}{4\mu R_{0}^{3}} \varepsilon b_{2}$$
 (5.11)

$$\tilde{B}_{2} = -\frac{E_{\infty}^{2}}{48\pi\mu R_{0}^{2}} 2\varepsilon(c_{2} + c_{4}) + \frac{\sigma}{4\mu R_{0}^{3}} \varepsilon c_{2}$$
(5.12)

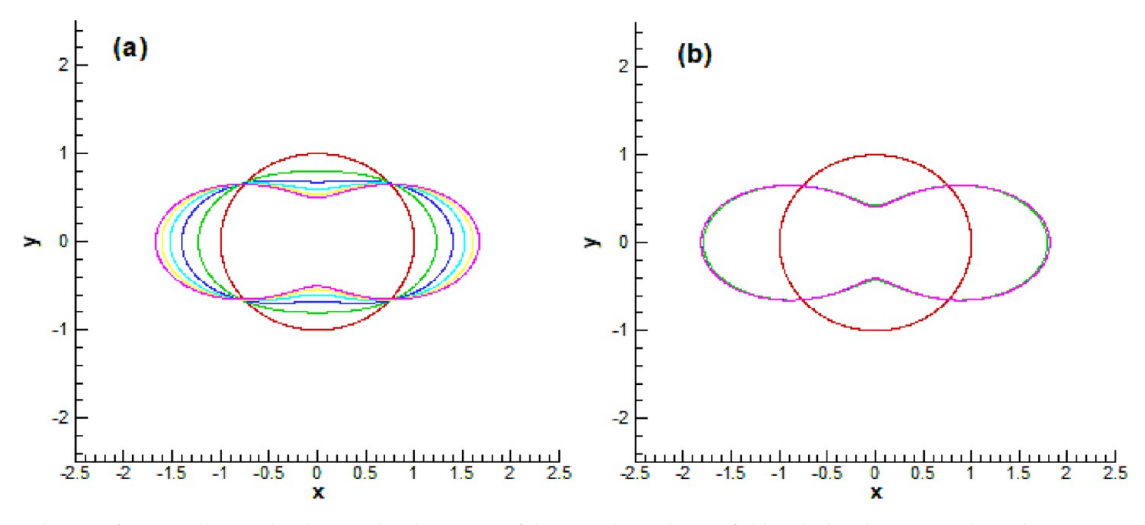


Figure 11. Evolution of an initially circular drop under the action of the stretching electric field with the electric Bond number $Bo_E = 10$ and surface tension. (a) Short-term evolution: the dimensionless time for the consecutive time moments $\tilde{t} = 0$, 0.99, 1.99, 2.99, 3.99, and 4.99 corresponding to the consecutive drop shapes depicted by curves with colors from red to pink, respectively. (b) Long-term evolution: the dimensionless time for consecutive time moments $\tilde{t} = 0$, 9.99, 19.99, 29.99, 39.99, and 49.99 corresponding to the consecutive drop shapes depicted by curves with colors from red to pink, respectively. Coordinates x and y are rendered dimensionless by R_0 .

$$\tilde{A}_{n} = -\frac{E_{\infty}^{2} \varepsilon}{16\pi \mu R_{0}^{n} (n+1)} \left[-(b_{n+2} + 2b_{n} + b_{n-2}) + (n+1)(b_{n+2} + b_{n}) + (n-1)(b_{n} + b_{n-2}) - \frac{4\pi}{Bo_{E}} (n^{2} - 1)b_{n} \right]$$
(5.13)

$$\tilde{B}_{n} = -\frac{E_{\infty}^{2} \varepsilon}{16\pi \mu R_{0}^{n} (n+1)} \left[-(c_{n+2} + 2c_{n} + c_{n-2}) + (n+1)(c_{n+2} + c_{n}) + (n-1)(c_{n} + c_{n-2}) - \frac{4\pi}{Bo_{E}} (n^{2} - 1)c_{n} \right]$$
(5.14)

In eqs 5.13 and 5.14, the electric Bond number is given by eq 4.2.

The next step is to consider the kinematic boundary condition at the drop surface. It would require the expression for the radial component of velocity v_r . The general expression for the latter was found by ref 19. Accounting for the fact that here v_r should be finite at r = 0 and using eqs 5.6, the expression for v_r reduces to

$$\nu_r = \sum_{n=2}^{\infty} (r^{n+1} + Dr^{n-1}) n(\tilde{A}_n \cos n\theta + \tilde{B}_n \sin n\theta)$$
(5.15)

The linearized kinematic boundary condition at the drop surface reads¹⁹

$$v_{r}|_{r=R_{0}} = R_{0}\varepsilon \frac{\partial Z}{\partial t} \tag{5.16}$$

Then, substituting eqs 4.4, 5.5, and 5.11–5.15 into eq 5.16, one finds the following system of the ordinary differential equations, which determine the dependence of the coefficients of the Fourier series in eq 4.2 for the surface perturbation:

$$\frac{\mathrm{d}\tilde{b}_0}{\mathrm{d}t} = \frac{\mathrm{d}\tilde{c}_1}{\mathrm{d}t} = \frac{\mathrm{d}\tilde{b}_1}{\mathrm{d}t} = 0 \tag{5.17}$$

$$\frac{\mathrm{d}\tilde{c}_{2}}{\mathrm{d}t} = \frac{E_{\infty}^{2}}{12\pi\mu} \left[2(\tilde{c}_{2} + \tilde{c}_{4}) - \frac{12\pi}{\mathrm{Bo}_{\mathrm{E}}} \tilde{c}_{2} \right]$$
(5.18)

$$\frac{d\tilde{b}_2}{dt} = \frac{E_{\infty}^2}{12\pi\mu} \left[1 + 2(\tilde{b}_2 + \tilde{b}_4) - \frac{12\pi}{Bo_E} \tilde{b}_2 \right]$$
 (5.19)

and for n > 3

$$\frac{\mathrm{d}\tilde{c}_{n}}{\mathrm{d}t} = \frac{E_{\infty}^{2}n}{8\pi\mu(n^{2}-1)} \left[-(\tilde{c}_{n+2}+2\tilde{c}_{n}+\tilde{c}_{n-2}) + (n+1)(\tilde{c}_{n+2}+\tilde{c}_{n}) + (n-1)(\tilde{c}_{n}+\tilde{c}_{n-2}) - \frac{4\pi}{\mathrm{Bo}_{\mathrm{E}}}(n^{2}-1)\tilde{c}_{n} \right]$$
(5.20)

$$\frac{d\tilde{b}_{n}}{dt} = \frac{E_{\infty}^{2}n}{8\pi\mu(n^{2}-1)} \left[-(\tilde{b}_{n+2} + 2\tilde{b}_{n} + \tilde{b}_{n-2}) + (n+1)(\tilde{b}_{n+2} + \tilde{b}_{n}) + (n-1)(\tilde{b}_{n} + \tilde{b}_{n-2}) - \frac{4\pi}{Bo_{E}}(n^{2}-1)\tilde{b}_{n} \right]$$
(5.21)

where $\tilde{b}_n = \varepsilon b_n$ and $\tilde{c}_n = \varepsilon c_n$.

The initial conditions for the system of eqs 5.17-5.21 corresponding to a circular drop are the following:

$$t = 0: \quad \tilde{b}_0 = \tilde{c}_n = \tilde{b}_n = 0, \quad \forall \ n \ge 1$$
 (5.22)

It should be emphasized that, in the system of eqs 5.17–5.21, only eq 5.19 for \tilde{b}_2 contains the order of 1 term on the right-hand side, $E_{\infty}^2/12\pi\mu$. Only this term is operational when the initial drop is circular, because even a circular drop is stretched by the imposed electric field (cf. Figure 11). This triggers growth of the coefficient \tilde{b}_2 , which makes the drop elliptical and, in turn, through eq 5.21 triggers growth of all coefficients \tilde{b}_n with even values of n. Note that even the largest coefficient \tilde{b}_2 still stays small for the linear approximation being formally valid during the time period given by eq 4.3.

On the other hand, as a result of the initial conditions in eq 5.22, eqs 5.17-5.21 yield the following solutions:

$$t > 0$$
: $\tilde{c}_n \equiv 0$, $\forall n \ge 1$;
 $\tilde{b}_0 \equiv 0$; $\tilde{b}_n \equiv 0$ for $n = 2k - 1$, $\forall k \ge 1$ (5.23)

Accordingly, rendering time dimensionless as

$$\tilde{t} = \frac{t}{\mu R_0 / \sigma} \tag{5.24}$$

the system of equations to solve reduces to

$$\frac{d\tilde{b}_{2}}{d\tilde{t}} = \frac{Bo_{E}}{12\pi} \left[1 + 2(\tilde{b}_{2} + \tilde{b}_{4}) - \frac{12\pi}{Bo_{E}} \tilde{b}_{2} \right]$$
(5.25)

and for n = 2k (with k > 1)

$$\frac{d\tilde{b}_{n}}{d\tilde{t}} = \frac{Bo_{E}n}{8\pi(n^{2}-1)} \left[-(\tilde{b}_{n+2} + 2\tilde{b}_{n} + \tilde{b}_{n-2}) + (n+1)(\tilde{b}_{n+2} + \tilde{b}_{n}) + (n-1)(\tilde{b}_{n} + \tilde{b}_{n-2}) - \frac{4\pi}{Bo_{E}}(n^{2}-1)\tilde{b}_{n} \right]$$
(5.26)

It is also expected that the highest harmonics corresponding to a sufficiently high value of $n \ge N + 2$ (where N is even and sufficiently large) would be suppressed by surface tension (i.e., $b_n \approx 0$ for $n \ge N + 2$), and thus, the system of eqs 5.25 and 5.26 could be truncated to the following equation:

$$\frac{d\tilde{b}_{N}}{d\tilde{t}} = \frac{Bo_{E}N}{8\pi(N^{2}-1)} \left[-(2\tilde{b}_{N} + \tilde{b}_{N-2}) + (N+1)\tilde{b}_{N} + (N-1)(\tilde{b}_{N} + \tilde{b}_{N-2}) - \frac{4\pi}{Bo_{E}}(N^{2}-1)\tilde{b}_{N} \right]$$
(5.27)

To find transient drop shapes, the system of eqs 5.25–5.27 is to be solved numerically using the Kutta–Merson method with the following initial conditions corresponding to an initial circle:

$$\tilde{t} = 0$$
: $\tilde{b}_n = 0$, $\forall n = 2k \text{ with } k \ge 1$ (5.28)

Also, according to eqs 4.1 and 4.4, the drop shape is found as

$$\tilde{R}(\theta, \,\tilde{t}) = 1 + \sum_{n_{\text{even}}=2}^{N} \tilde{b}_{n}(\tilde{t}) \cos n\theta \tag{5.29}$$

where the radius is rendered dimensionless by R_0 . The Cartesian coordinates of the drop contour are found as $\tilde{x} = \tilde{R} \cos \theta$ and $\tilde{y} = \tilde{R} \sin \theta$ (rendered dimensionless by R_0).

It should be emphasized that the drop area change corresponding to eq 5.29 would be of the order of \tilde{b}_n^2 , which means that it is negligibly small in the linear approximation.

6. STEADY-STATE DROP SHAPE

At sufficiently low values of the electric Bond number, the transient evolution of a drop stretched by the imposed electric field will lead to a steady state, in which the restoring action of the surface tension will be able to fully (and pointwise) compensate for the stretching action of the electric Maxwell stresses at the drop surface.

The steady-state solutions are sought for eqs 5.25, 5.26 (with $4 \le n \le N - 2$), and 5.27, with the time derivatives being 0; i.e., the following system of linear algebraic equations is to be solved:

$$1 + 2(\tilde{b}_2 + \tilde{b}_4) - \frac{12\pi}{Bo_E} \tilde{b}_2 = 0$$
(6.1)

$$-(\tilde{b}_{n+2} + 2\tilde{b}_n + \tilde{b}_{n-2}) + (n+1)(\tilde{b}_{n+2} + \tilde{b}_n)$$

$$+ (n-1)(\tilde{b}_n + \tilde{b}_{n-2}) - \frac{4\pi}{\mathrm{Bo}_{\mathrm{E}}} (n^2 - 1)\tilde{b}_n = 0$$
(6.2)

$$\tilde{b}_{N-2}(N-2) + \tilde{b}_N \left[2(N-1) - \frac{4\pi}{\text{Bo}_E} (N^2 - 1) \right] = 0$$
(6.3)

Equation 6.2 with $4 \le n \le N-2$ corresponds to the system of algebraic equations with a three-diagonal matrix. Solutions of this system are found using the Thomas algorithm⁵³ in the following form:

$$\tilde{b}_n = L_n \tilde{b}_{n+2} + P_n \tag{6.4}$$

where the coefficients L_n and P_n (for any even n) are to be found.

When eq 6.4 is substituted in eq 6.1, one finds the following first pair of the coefficients:

$$L_2 = -\frac{2}{2 - 12\pi/\text{Bo}_E}, \quad P_2 = -\frac{1}{2 - 12\pi/\text{Bo}_E}$$
 (6.5)

Then, substituting eq 6.4 into eq 6.2, one finds the following recurrent formulas required to find all of the coefficients L_n and P_n (for $4 \le n \le N - 2$) with the ascending even values of n:

$$L_n = -\frac{n}{L_{n-2}(n-2) + 2(n-1) - 4\pi(n^2 - 1)/Bo_E}$$
(6.6)

$$P_{n} = -\frac{P_{n-2}(n-2)}{L_{n-2}(n-2) + 2(n-1) - 4\pi(n^{2}-1)/Bo_{E}}$$
(6.7)

After that, substituting eq 6.4 into eq 6.3, one fully finds the coefficient b_N as

$$\tilde{b}_N = -\frac{P_{N-2}(N-2)}{L_{N-2}(N-2) + 2(N-1) - 4\pi(N^2 - 1)/Bo_E}$$
(6.8)

and then the double sweep is finalized as

$$\tilde{b}_n = L_n \tilde{b}_{n+2} + P_n, \quad N-2 \ge n \ge 2$$
 (6.9)

which allows one to find the succession of all of the other coefficients b_n with descending even values of n.

It should be emphasized that eqs 6.6–6.8 show that that, at large n (and N), the coefficients L_n and P_n tend to 0 as well as $\tilde{b}_N \to 0$. Accordingly, eq 6.9 shows that, in the steady-state solutions, all of the coefficients \tilde{b}_n are small (under the condition of eq 4.3) and the perturbed drop shape is mostly determined by the coefficients with the lowest values of n, \tilde{b}_2 , and maybe \tilde{b}_4 .

7. EXAMPLES OF TRANSIENT AND STEADY-STATE SOLUTIONS

The transient solution at the electric Bond number $Bo_E = 10$ predicted by solving numerically the system of eqs 5.25-5.27 is illustrated in Figure 11, where in panel a in the short-time range, the drop shape varies significantly, whereas in panel b at longer times, the drop shape approaches the steady-state and saturates. This steady-state shape can also be predicted analytically using eqs 6.5-6.9, as depicted in Figure 12.

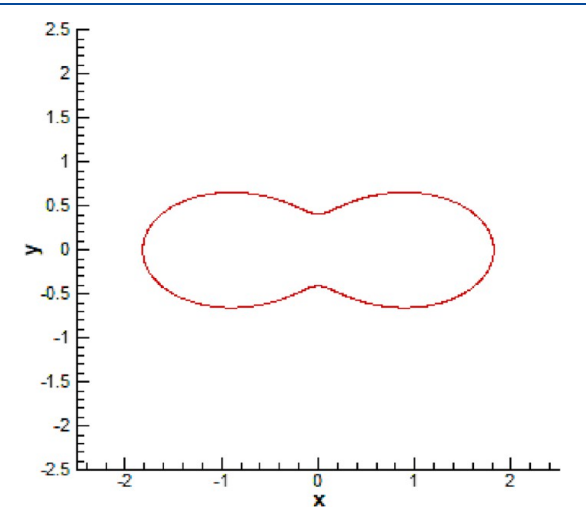


Figure 12. Steady-state shape of the drop under the action of the stretching electric field with the electric Bond number $Bo_E = 10$ and surface tension. Coordinates x and y are rendered dimensionless by R_0 .

It should be emphasized that according to eq 4.3 the time period when the linear approximation is formally valid is $\tilde{t} < 12\pi/\mathrm{Bo_E}$, which yields $\tilde{t} < 3.8$ for the value of $\mathrm{Bo_E} = 10$. Therefore, the predicted dimpled shape of the drop corresponding to $\tilde{t} = 4.99$ in Figure 11a is clearly outside the range of formal validity of the linear approximation used to find the analytical solution. Still, it is luring to check the large-perturbation predictions of the analytical solution constructed in sections 4–6 versus the nonlinear numerical solution and the experimental data, which is performed below in this section and in section 8, respectively.

At $Bo_E = 20$, steady state is already impossible and the drop will be teared apart by the electric Maxwell stresses; i.e., this value of the electric Bond number is already supercritical. The drop shape evolves as shown in Figure 13 using numerical solution of the system of eqs 5.25–5.27. After the moment \tilde{t} = 1.44 (\tilde{t} < 1.87 is the ultimate time limit according to eq 4.3 in this case), the drop will be rapidly teared apart. No steady-state solution exists in this case. Note that in a very insightful work of Crowdy, 40 deformation of an incompressible equipotential bubble under the action of a horizontal uniform-at-infinity electric field was considered in the creeping-flow approximation. The resulting exact numerical solution for the bubble shape was constructed using the problem complexization and conformal mapping. It revealed that, at a certain supercritical value of the electric Bond number, steady-state solutions cease to exist and the bubble is teared apart into two bubbles very similarly to the scenario depicted in Figure 13. The experimental observation, which confirms prediction of the

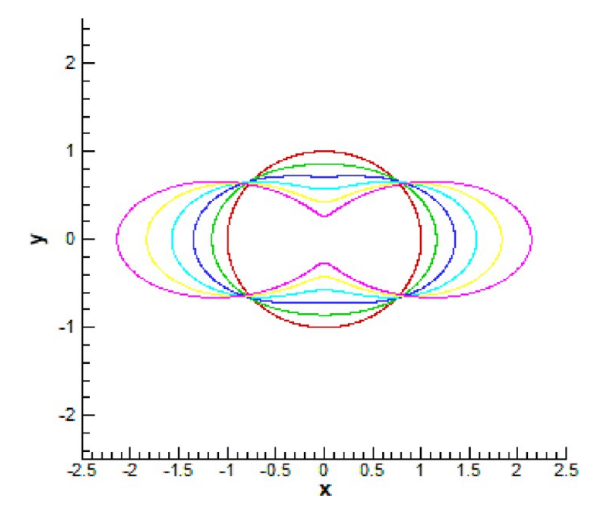


Figure 13. Evolution of an initially circular drop under the action of the stretching electric field with the electric Bond number $Bo_E = 20$ and surface tension. The dimensionless time for the consecutive time moments $\tilde{t} = 0$, 0.28, 0.57, 0.86, 1.15, and 1.44 corresponding to the consecutive drop shapes depicted by curves with colors from red to pink, respectively. Coordinates x and y are rendered dimensionless by R.

dimple formation and tearing apart of drops by the electric field, is discussed in section 8.

It has already been noted that the results shown in Figures 11–13 extend beyond the range of the formal validity of the linearized, small-perturbation theory of sections 4–6. Nevertheless, direct comparison of similar results to the experimental data reveals that they, indeed, can be reliable and accurate far beyond their formal range of validity (cf. Figure 3 in ref 19 and section 6.9 in ref 12), and additional comparisons of this type are provided in this section and the following section 8.

The Fourier series coefficients \tilde{b}_2 , \tilde{b}_4 , and \tilde{b}_6 plotted versus the dimensionless time \tilde{t} in Figure 14 ascertain how the significance of the coefficient \tilde{b}_n decreases drastically with an increase in the subscript n (cf. the last paragraph in section 6). The drive to growth delivered to \tilde{b}_2 by the electric stretching

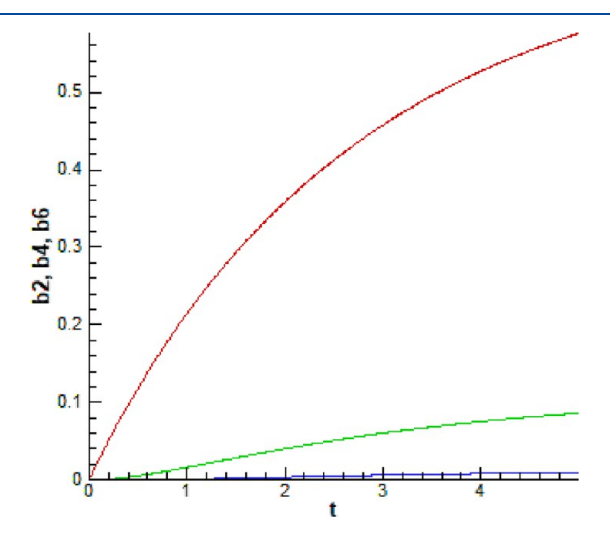


Figure 14. Coefficients \tilde{b}_2 , \tilde{b}_4 , and \tilde{b}_6 versus the dimensionless time \tilde{t} . The coefficients are rendered dimensionless by R_0 . The electric Bond number $\mathrm{Bo_E}=10$, and the results correspond to those of Figure 11a. The red curve shows \tilde{b}_2 ; the green curve shows \tilde{b}_4 ; and the blue curve shows \tilde{b}_6 .

force (cf. the order of 1 term on the right-hand side in eq 5.25) determines its significant growth, as in Figure 14. Simultaneously, eq 5.26 redistributes the growth of b_2 to higher harmonics. However, the higher the harmonic, the stronger the smoothing effect of the surface tension (cf. the last term on the right-hand side in eq 5.26), which suppresses growth of the higher harmonics. Accordingly, the theory of sections 4-6 does not leave a place for the appearance of such shortwavelength details as, for example, fingering.

It is instructive to compare the linearized analytical steadystate solution of eqs 6.5-6.9 to the numerical simulation of the corresponding fully nonlinear problem for a 2D drop under the action of surface tension and an imposed stretching electric field. The numerical solution is found using COMSOL. The incompressible Navier-Stokes equations are solved in the framework of the phase field modeling (PFM). The free surface of the drop corresponds to the phase field parameter equal to 0.5. The domain is taken as 15 mm \times 15 mm with a 3 mm drop located at the center, with the high voltage being applied at the right-hand-side boundary, while the left-handside boundary is grounded. It should be emphasized that, in these simulations, the drop is not a prefect conductor; however, the potential difference across it is negligibly small compared to the overall potential difference applied. Accordingly, the drop is practically equipotential.

The numerically predicted steady-state drop shapes are compared to the analytical predictions for two values of the electric Bond number in Figure 15. The agreement is very

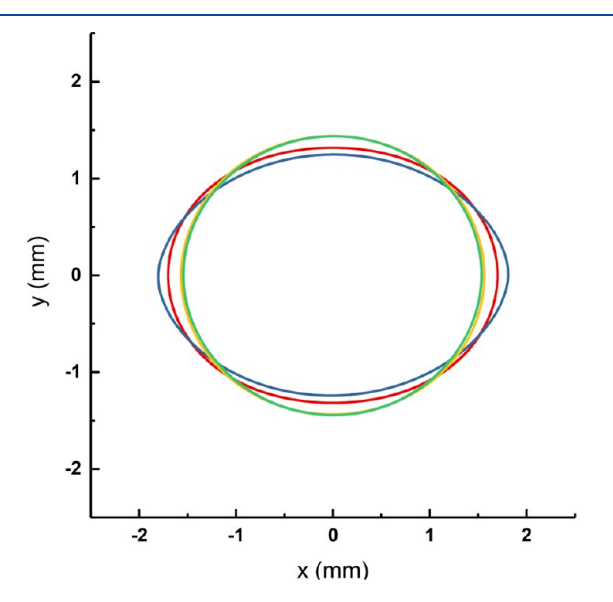


Figure 15. Comparison of the numerically and analytically predicted steady-state drop shapes. The yellow and red lines depict the analytically predicted drop shapes with Bo_E = 1.483 and 3.796, respectively, and the green and blue lines depict the numerically predicted drop shapes with Bo_E = 1.483 and 3.796, respectively.

good, even though quite significant drop deformations are involved. As expected, the agreement is better for the lower value of Bo_E. At the higher value of Bo_E, the analytical solution slightly underestimates the drop stretching. It should be emphasized that the PFM simulations required intensive mesh quality for the interface tracking and mass conservation, and they are also strongly dependent upon selection of the artificial parameter, namely, the mobility tuning parameter. Both requirements make it difficult for case verification. As a result,

the present analytical solution can also serve as a useful benchmark case for such time-consuming numerical simulations.

8. RESULTS AND DISCUSSION: COMPARISON OF THE THEORY TO EXPERIMENTAL DATA

8.1. Drop Impact Case. The steady-state drop contours observed on the polypropylene substrate, which were recorded in the images in Figure 2 and depicted in Figure 3 are compared to the theoretical predictions in Figure 16 for voltages of 4.5, 5, 7, 9, and 10 kV. The comparison reveals a fairly good agreement of the analytical prediction of eqs 6.5-6.9 with the experimental data in the entire voltage range up to the voltage of 10 kV, corresponding to the maximum drop stretching along the field lines in Figure 16e.

The comparison in Figure 16 shows that, in this case, the 2D theory, which completely disregards the 3D effects and the influence of the substrate, is sufficiently accurate despite these simplifying assumptions. Note also that we have found experimentally that the gold oak aniline dye incorporates both anion- and cation-like pigments. The electrical conductivity of regular water is already relatively high, and the dye effect would increase it even more. In any case, the charge relaxation time in both cases would be on the scale of 1 μ s, which is at least 3 orders of magnitude lower than the characteristic drop impact time. Accordingly, the theoretical assumption of fluid to be a perfect conductor holds for regular water or water-aniline dye. The effect of the dye pigments (at the concentration of 0.1 wt %) on surface tension of water is presumably not very strong, as the data on the surface tension of seawater at different salinity levels imply.⁵

8.2. Softly Deposited Drop Case. The steady-state drop contours measured on the polypropylene substrate using the images in Figures 4 and 6 and depicted in Figures 7 and 8 are compared to the theoretical predictions of eqs 6.5-6.9 in Figure 17. A similar comparison to the data on the parafilm surface from Figures 6 and 9 is presented in Figure 18. The results on the polypropylene surface reveal fairly good agreement between the theory and experiment only at the lower voltages of 6 and 7 kV in panels a and b of Figure 16, respectively. However, the theory underpredicts the maximum drop deformation, which becomes especially visible at 10.5 kV in Figure 17e. This reveals the effect of polypropylene with higher wettability in comparison to parafilm (cf. Figure S1 in Supporting Information). Also, polypropylene seemingly reveals a stronger electrowettability effect than parafilm. All of these facilitate drop stretching on polypropylene above the limit corresponding to the theoretically accounted effect of the electric Maxwell stresses.

On the other hand, a comparison of the theory to the data on less wettable parafilm reveals good agreement, as shown in Figure 18. In the case of parafilm, the effects of the substrate wettability are negligibly small compared to the effect of the pulling electric Maxwell stresses, which makes the predictions of the 2D theory accurate. The latter is also true despite the potential 3D effects, with friction losses at the drop footprint in contact with the substrate and additional friction losses at the moving contact line when the drop evolves to the steady-state shape. Note, however, that the experimental data for drops softly deposited on parafilm seemingly reveal the maximum stretching along the field lines for 10 kV (Figure 18c) rather than for 10.5 kV (Figure 18d), whereas the theory predicts a monotonously increasing stretching with voltage.

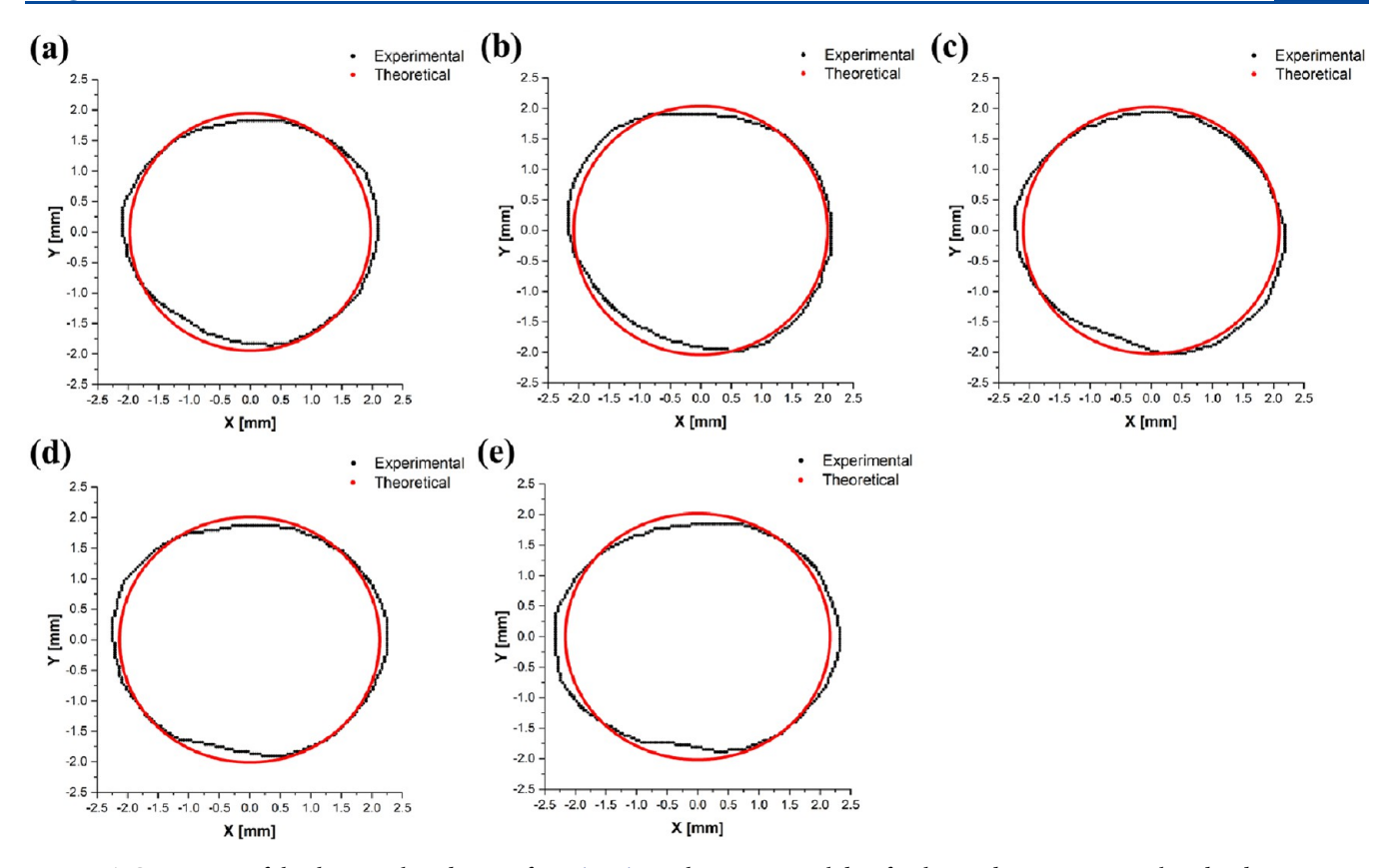


Figure 16. Comparison of the theoretical prediction of eqs 6.5-6.9 to the experimental data for the steady-state water—aniline dye drop contours measured on the polypropylene substrate with electric fields of (a) 4.5 kV, (b) 5 kV, (c) 7 kV, (d) 9 kV, and (e) 10 kV. These voltages correspond to electric field strengths of 3.0×10^5 , 3.33×10^5 , 4.67×10^5 , 6.0×10^5 , and $6.67 \times 10^5 \text{ V/m}$, respectively. The left-hand-side electrode is the anode, and the right-hand-side electrode is grounded (the cathode). The Cartesian coordinates on the substrate are denoted as x (in the field direction) and y. The experimental data are shown by black symbols, while the theoretical predictions are shown by red lines. The drop was deposited by impact.

Note also that, in the case of parafilm, the water static contact angle decreased from 100.4° at 0 kV to 82.7° at 10.5 kV, as mentioned above. Accordingly, for the cases of high enough applied voltages, the contact angles were less than 90° and the droplet footprints on parafilm were fully visible in the top view. On the other hand, in the cases of contact angles greater than 90°, the difference between the droplet footprint and its diameter in the top view on parafilm is on the scale of micrometers, which, in turn, means very few pixels of difference in the images taken for analysis using top and side views. For this reason, the possible errors associated with imaging the droplet footprint from above in the latter cases are negligibly small and could not considerably affect the results used for comparison to the theoretical predictions.

8.3. Tearing the Drop Apart in the Supercritical Electric Field. Viscous friction of stretching drop on a substrate is one of the two main factors that differs in the experiment and the 2D theory. Such a friction can be dramatically diminished by depositing a thin layer of silicone oil on the parafilm surface and then using it as a substrate for a drop. An experiment of this type was conducted using glycerol as a working fluid. Figure 19 reveals that, in such an experiment where the no-slip condition at the substrate surface was, essentially, eliminated, a transient drop evolution corresponding to the effect of the supercritical electric field is revealed. Specifically, the drop develops a dimple and is teared apart by the electric field in qualitative agreement with the predictions of the 2D theory illustrated in Figure 13 as well as with similar

predictions for bubbles subjected to a stretching electric field. ⁴⁰ It should be emphasized that this type of drop breakup differs from the electrical instability-driven jetting at drop tips, followed by capillary breakup of the jets and formation of multiple tiny drops. ⁵⁵

9. CONCLUSION

The creeping-flow theory of 2D Stokesian drops was developed and compared and also validated experimentally to steady-state drops under the action of surface tension and the subcritical electric field on different dielectric surfaces. The observations of the evolution of water-aniline dye drops after an impact from the height of 12.5 cm onto polypropylene revealed that the electric field strength of $6.67 \times 10^5 \text{ V/m}$ corresponding to the applied voltage of 10 kV stretched the drop and increased its steady-state area compared to the case without voltage by 19.8% (the footprint in the top view). This reveals significant 3D effects in drop spreading on the polypropylene substrate, which is attributed to its relative wettability. Despite this fact, the linearized 2D theory developed in this work successfully describes the experimental data for the steady-state water-aniline dye drops after an impact from the height of 12.5 cm onto polypropylene for all applied voltages of 4.5, 5, 7, 9, and 10 kV.

The experimental measurements with a softly deposited sessile drop of water—aniline dye on polypropylene revealed that electric field strengths of 6×10^5 , 7×10^5 , 9×10^5 , 10×10^5 , and 10.5×10^5 V/m corresponding to applied voltages of

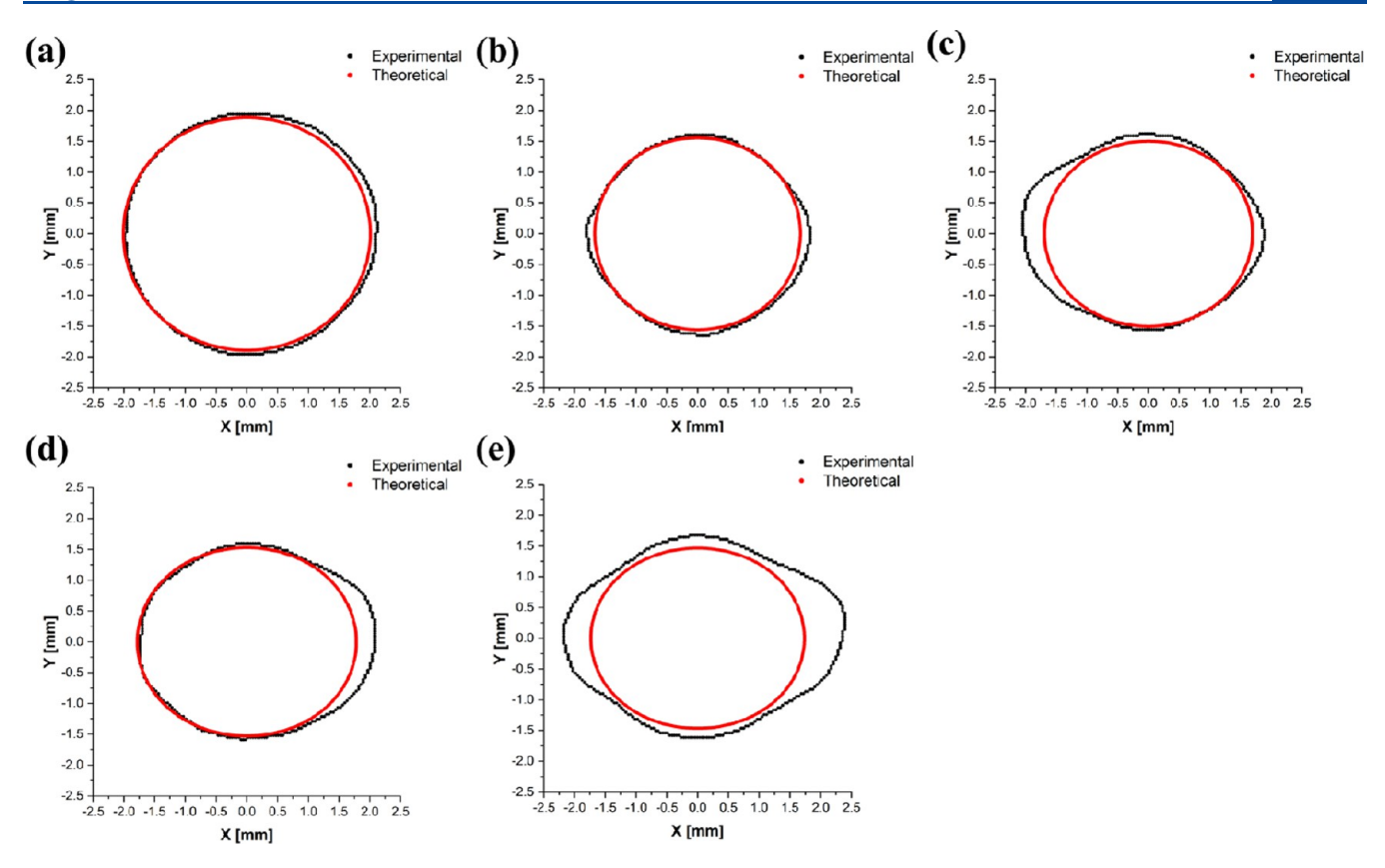


Figure 17. Comparison of the theoretical prediction of eqs 6.5-6.9 to the experimental data for the steady-state water—aniline dye drop contours measured on the polypropylene substrate with electric fields of (a) 6 kV, (b) 7 kV, (c) 9 kV, (d) 10 kV, and (e) 10.5 kV. The corresponding electric field strengths are 6×10^5 , 7×10^5 , 9×10^5 , 10×10^5 , and 10.5×10^5 V/m, respectively. The left-hand-side electrode is the anode, and the right-hand-side electrode is grounded (the cathode). The Cartesian coordinates on the substrate are denoted as x (in the field direction) and y. The experimental data are shown by black symbols, while the theoretical predictions are shown by red lines. The drop was deposited softly.

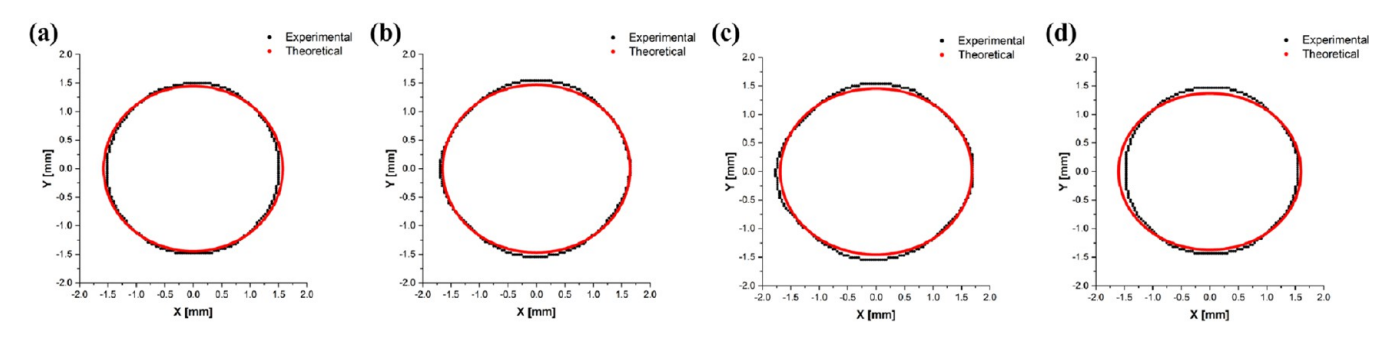


Figure 18. Comparison of the theoretical prediction of eqs 6.5–6.9 to the experimental data for the steady-state water—aniline dye drop contours measured on the parafilm substrate with electric fields of (a) 8 kV, (b) 9 kV, (c) 10 kV, and (d) 10.5 kV, which correspond to electric field strengths of 8×10^5 , 9×10^5 , 10×10^5 , and 10.5×10^5 V/m, respectively. The left-hand-side electrode is the anode, and the right-hand-side electrode is grounded (the cathode). The Cartesian coordinates on the substrate are denoted as x (in the field direction) and y. The experimental data are shown by black symbols, while the theoretical predictions are shown by red lines. The drop was deposited softly.

6, 7, 9, 10, and 10.5 kV, respectively, stretched the drops along the field lines and increased their steady-state average footprint areas compared to the case without voltage applied by 5.6, 5.8, 12.7, 13.6, and 20.5%, respectively. This is also related to a relative wettability of polypropylene by water—aniline dye drops, which is also enhanced by the additional electrowettability. Because of the pronounced effect of the substrate wettability in this case, the linearized 2D theory developed in this work significantly underpredicts stretching of the softly deposited water—aniline dye drops on the polypropylene substrate.

Additionally, the observations of a softly deposited sessile drop of water—aniline dye on the parafilm substrate revealed that electric field strengths of 8×10^5 , 9×10^5 , 10×10^5 , and 10.5×10^5 V/m corresponding to applied voltages of 8, 9, 10, and 10.5 kV, respectively, stretched the drops and increased their steady-state areas compared to the case without voltage by only 0.71, 4.7, 7.7, and 2.6%, respectively. These results show that drop stretching on the parafilm surface is close to the 2D flow, which is related to the fact that parafilm is relatively non-wettable by water—aniline dye drops, and thus, wettability does not play any role in drop stretching compared to the electrically driven stretching. This makes the experiments on



Figure 19. Glycerol drop on parafilm coated with a thin layer of a low-viscosity silicone oil and subjected to the voltage of 7 kV.

drop stretching on parafilm prone to comparison to the 2D theory developed in this work, and the theoretical predictions agree with the experimental data fairly well in this case.

The results reveal that the present 2D creeping-flow theory is in good agreement with the experimental data and nonlinear numerical results for drops on non-wettable substrates (where a drop is raised over the substrate and, thus, differs from a thin lubrication model) subjected to a subcritical electric field. The present 2D model is also in good qualitative agreement with experimental observations with droplets on substrates where the no-slip condition is removed and a supercritical electric field is applied. In the latter case drops developed a dimple in the middle and teared apart.

ASSOCIATED CONTENT

Supporting Information

The Supporting Information is available free of charge at https://pubs.acs.org/doi/10.1021/acs.langmuir.1c01015.

Equilibrium contact angle of water—aniline dye with no voltage applied on the (a) polypropylene substrate and (b) parafilm substrate (Figure S1) (PDF)

AUTHOR INFORMATION

Corresponding Author

Alexander L. Yarin — Department of Mechanical and Industrial Engineering, University of Illinois at Chicago, Chicago, Illinois 60607-7022, United States; oorcid.org/0000-0001-8032-2525; Phone: 312-996-3472; Email: ayarin@uic.edu; Fax: 312-413-0447

Authors

Rafael Granda – Department of Mechanical and Industrial Engineering, University of Illinois at Chicago, Chicago, Illinois 60607-7022, United States

Jevon Plog – Department of Mechanical and Industrial Engineering, University of Illinois at Chicago, Chicago, Illinois 60607-7022, United States

Gen Li – Department of Mechanical and Industrial Engineering, University of Illinois at Chicago, Chicago, Illinois 60607-7022, United States

Vitaliy Yurkiv — Department of Mechanical and Industrial Engineering, University of Illinois at Chicago, Chicago, Illinois 60607-7022, United States; orcid.org/0000-0002-3407-891X

Farzad Mashayek – Department of Mechanical and Industrial Engineering, University of Illinois at Chicago, Chicago, Illinois 60607-7022, United States; orcid.org/0000-0003-1187-4937

Complete contact information is available at: https://pubs.acs.org/10.1021/acs.langmuir.1c01015

Note:

The authors declare no competing financial interest.

ACKNOWLEDGMENTS

The authors acknowledge the financial support from the National Science Foundation Award CBET-1806497.

REFERENCES

- (1) Karniadakis, G.; Beskok, A.; Aluru, N. Microflows and Nanoflows. Fundamentals and Simulation; Springer: Berlin, Germany, 2005; DOI: 10.1007/0-387-28676-4.
- (2) Mugele, F.; Baret, J.-C. Electrowetting: From basics to applications. J. Phys.: Condens. Matter 2005, 17, R705-R774.
- (3) Mugele, F.; Heikenfeld, J. Electrowetting: Fundamental Principles and Practical Applications; Wiley-VCH: Weinheim, Germany, 2019.
- (4) Yarin, A. L. Wetting for self-healing, and electrowetting for additive manufacturing. *Curr. Opin. Colloid Interface Sci.* **2021**, *51*, 101378.
- (5) Yarin, A. L.; Roisman, I. V.; Tropea, C. Collision Phenomena in Liquids and Solids; Cambridge University Press: Cambridge, U.K., 2017; DOI: 10.1017/9781316556580.
- (6) Lee, M. W.; Latthe, S. S.; Yarin, A. L.; Yoon, S. S. Dynamic electrowetting-on-dielectric (DEWOD) on unstretched and stretched Teflon. *Langmuir* **2013**, *29*, 7758–7767.
- (7) Yurkiv, V.; Yarin, A. L.; Mashayek, F. Modeling of droplet impact onto polarized and nonpolarized dielectric surfaces. *Langmuir* **2018**, 34, 10169–10180.
- (8) Plog, J.; Löwe, J.-M.; Jiang, Y.; Pan, Y.; Yarin, A. L. Drop control by electrowetting in 3D printing. *Langmuir* **2019**, *35*, 11023–11036.
- (9) Plog, J.; Jiang, Y.; Pan, Y.; Yarin, A. L. Electrostatically-assisted direct ink writing for additive manufacturing. *Addit. Manuf.* **2021**, 39, 101644.
- (10) Löwe, J.-M.; Plog, J.; Jiang, Y.; Pan, Y.; Yarin, A. L. Drop deposition affected by electrowetting in direct ink writing process. *J. Appl. Phys.* **2019**, *126*, 035302.
- (11) Mhatre, S.; Vivacqua, V.; Ghadiri, M.; Abdullah, A. M.; Al-Marri, M. J.; Hassanpour, A.; Hewakandamby, B.; Azzopardi, B.; Kermani, B. Electrostatic phase separation: A review. *Chem. Eng. Res. Des.* **2015**, *96*, 177–195.

- (12) Yarin, A. L.; Pourdeyhimi, B.; Ramakrishna, S. Fundamentals and Applications of Micro- and Nanofibers; Cambridge University Press: Cambridge, U.K., 2014; DOI: 10.1017/CBO9781107446830.
- (13) Chen, L.; Bonaccurso, E. Electrowetting—From statics to dynamics. Adv. Colloid Interface Sci. 2014, 210, 2–12.
- (14) Xie, G.; He, F.; Liu, X.; Si, L.; Guo, D. Sessile multidroplets and salt droplets under high tangential electric fields. *Sci. Rep.* **2016**, *6*, 25002.
- (15) Yang, D.; Sun, Y.; He, L.; Luo, X.; Lü, Y.; Yin, H.; Xia, X.; Zhang, H. Coalescence characteristics of silica nanoparticle-laden droplets with a planar interface under direct current electric field. *Chem. Eng. Res. Des.* **2018**, *140*, 128–141.
- (16) Plog, J.; Jiang, Y.; Pan, Y.; Yarin, A. L. Coalescence of sessile droplets driven by electric field in the jetting-based 3D printing framework. *Exp. Fluids* **2021**, *62*, 56.
- (17) Langlois, W. E. Slow Viscous Flow; The Macmillan Company: New York, 1964.
- (18) Happel, J.; Brenner, H. Low Reynolds Number Hydrodynamics; Kluwer: Dordrecht, Netherlands, 1991.
- (19) Yarin, A. L. Surface-tension-driven low Reynolds number flows arising in optoelectronic technology. *J. Fluid Mech.* **1995**, 286, 173–200
- (20) Muskhelishvili, N. I. Some Basic Problems of the Mathematical Theory of Elasticity; Noordhoff International Publishing: Leyden, Netherlands, 1975.
- (21) England, A. H. Complex Variable Methods in Elasticity; John Wiley & Sons: New York, 1971.
- (22) Cherepanov, G. P. Mechanics of Brittle Fracture; McGraw Hill: New York, 1979.
- (23) Galin, L. A. *Contact Problems*; Springer: Berlin, Germany, 2008; DOI: 10.1007/978-1-4020-9043-1.
- (24) Smirnov, V. I. A Course of Higher Mathematics; Pergamon Press: Elmsford, NY, 1964; DOI: 10.1016/C2013-0-02283-9.
- (25) Lavrentiev, M. A.; Shabat, B. V. Methods of the Theory of Functions of Complex Variable; Nauka: Moscow, Russia, 1973 (in Russian).
- (26) Barenblatt, G. I. Flow, Deformation and Fracture; Cambridge University Press: Cambridge, U.K., 2014; DOI: 10.1017/CBO9781139030014.
- (27) Zhang, W.; Staszel, C.; Yarin, A. L.; Shim, E.; Pourdeyhimi, B. Point-bonded polymer nonwovens and their rupture in stretching. *Polymer* **2018**, *146*, 209–221.
- (28) Kolbasov, A.; Sinha-Ray, S.; Yarin, A. L. Theoretical and experimental study of punched laminate composites protected by outer paper layer. *J. Mech. Phys. Solids* **2019**, *128*, 117–136.
- (29) Richardson, S. Two-dimensional bubbles in slow viscous flow. *J. Fluid Mech.* **1968**, 33, 475–493.
- (30) Richardson, S. Two-dimensional slow viscous flows with time dependent free boundaries driven by surface tension. *Eur. J. Appl. Math.* **1992**, *3*, 193–207.
- (31) Richardson, S. Plane Stokes flow with time-dependent free boundaries in which the fluid occupies a doubly connected region. *Eur. J. Appl. Math.* **2000**, *11*, 249–269.
- (32) Hopper, R. W. Coalescence of two equal cylinders: Exact results for creeping viscous flow driven by capillarity. *J. Am. Ceram. Soc.* **1984**, *67*, C-262–C-264.
- (33) Hopper, R. W. Plane Stokes flow driven by capillarity on a free surface. *J. Fluid Mech.* **1990**, 213, 349–375.
- (34) Hopper, R. W. Plane Stokes flow driven by capillarity on a free surface. *J. Fluid Mech.* **1991**, 230, 355–364.
- (35) Hopper, R. W. Stokes flow of a cylinder and half-space driven by capillarity. *J. Fluid Mech.* **1992**, 243, 171–181.
- (36) Tanveer, S.; Vasconcelos, G. L. Time-Evolving Bubbles in Two-Dimensional Stokes Flow; Institute for Computer Applications in Science and Engineering, NASA Langley Research Center: Hampton, VA, 1994; NASA Contractor Report 194998, ICASE Report 94-90.
- (37) Crowdy, D. G.; Tanveer, S. A theory of exact solutions for plane viscous blobs. *J. Nonlinear Sci.* **1998**, *8*, 261–279.

- (38) Crowdy, D. G.; Tanveer, S. A theory of exact solutions for annular viscous blobs. *J. Nonlinear Sci.* 1998, 8, 375–400.
- (39) Crowdy, D. G. Viscous sintering of unimodal and bimodal cylindrical packings with shrinking pores. *Eur. J. Appl. Math.* **2003**, *14*, 421–445
- (40) Crowdy, D. Conducting drops subject to electric fields in 2D Stokes flows. *IMA J. Appl. Math.* **2008**, 73, 740–758.
- (41) Sankaran, A.; Yarin, A. L. Evaporation-driven thermocapillary Marangoni convection in liquid layers of different depths. *Int. J. Heat Mass Transfer* **2018**, 122, 504–514.
- (42) Rayleigh, Lord. On the equilibrium of liquid conducting masses charged with electricity. The London, Edinburgh, and Dublin Philosophical Magazine and Journal of Science 1882, 14, 184–186.
- (43) Feng, J. Q. Electrically charged conducting drops revisited. Q. Appl. Math. 1997, 55, 525-536.
- (44) Taylor, G. I. Studies in electrohydrodynamics. I. The circulation produced in a drop by electrical field. *Proc. R. Soc. London, Ser. A* **1966**, 291, 159–166.
- (45) Saville, D. A. Electrohydrodynamics: The Taylor-Melcher leaky dielectric model. *Annu. Rev. Fluid Mech.* **1997**, 29, 27–64.
- (46) Ajayi, O. O. A note on Taylor's electrohydrodynamic theory. *Proc. R. Soc. London, Ser. A* **1978**, 364, 499–507.
- (47) Feng, J. Q. A 2D electrohydrodynamic model for electrorotation of fluid drops. J. Colloid Interface Sci. 2002, 246, 112–121.
- (48) Esmaeeli, A.; Sharifi, P. Transient electrohydrodynamics of a liquid drop. *Phys. Rev. E* **2011**, *84*, 036308.
- (49) Das, D.; Saintillan, D. A three-dimensional small-deformation theory for electrohydrodynamics of dielectric drops. *J. Fluid Mech.* **2021**, *914*, A22.
- (50) Sedov, L. I. Similarity and Dimensional Methods in Mechanics, 10th ed.; CRC Press: Boca Raton, FL, 1993.
- (51) Yarin, L. P. The Pi-Theorem: Applications to Fluid Mechanics and Heat and Mass Transfer; Springer: Berlin, Germany, 2012; DOI: 10.1007/978-3-642-19565-5.
- (52) Landau, L. D.; Lifshitz, E. M. Electrodynamics of Continuous Media; Pergamon Press: Oxford, U.K., 1984.
- (53) Datta, B. N. *Numerical Linear Algebra and Applications*, 2nd ed.; Society for Industrial and Applied Mathematics (SIAM): Philadelphia, PA, 2010; p 162, DOI: 10.1137/1.9780898717655.
- (54) Nayar, K. G.; Panchanathan, D.; McKinley, G. H.; Lienhard, J. H. Surface tension of seawater. *J. Phys. Chem. Ref. Data* **2014**, 43, 043103.
- (55) Duft, D.; Achtzehn, T.; Muller, R.; Huber, B. A.; Leisner, T. Coulomb fission: Rayleigh jets from levitated microdroplets. *Nature* **2003**, *421*, 128–128.